

# Fundamental differences in the radio properties of red and blue quasars: evolution strongly favoured over orientation

L. Klindt,<sup>1</sup><sup>\*</sup> D. M. Alexander,<sup>1</sup> D. J. Rosario,<sup>1</sup> E. Lusso,<sup>1</sup> & S. Fotopoulou<sup>1</sup>

<sup>1</sup>*Centre for Extragalactic Astronomy, Department of Physics, Durham University, Durham DH1 3LE, UK*

Accepted XXX. Received YYY; in original form ZZZ

## ABSTRACT

A minority of the optically selected quasar population are red at optical wavelengths due to the presence of dust along the line-of-sight. A key focus of many red quasar studies is to understand their relationship with the overall quasar population: are they blue quasars observed at a (slight) inclination angle or do they represent a transitional phase in the evolution of quasars? Identifying fundamental differences between red and blue quasars is key to discriminate between these two paradigms. To robustly explore this, we have uniformly selected quasars from the Sloan Digital Sky Survey with mid-infrared counterparts, carefully controlling for luminosity and redshift effects. We take a novel approach to distinguish between colour-selected quasars in the redshift range of  $0.2 < z < 2.4$  by constructing redshift-sensitive  $g^* - i^*$  colour cuts. From cross-matching this sample to the Faint Images of the Radio Sky at Twenty-centimeters (FIRST) survey, we have found a factor  $\approx 3$  larger fraction of radio-detected red quasars with respect to that of blue quasars. Through a visual inspection of the FIRST images and an assessment of the radio luminosities (rest-frame  $L_{1.4 \text{ GHz}}$  and  $L_{1.4 \text{ GHz}}/L_{6 \mu\text{m}}$ ) we find that the radio-detection excess for red quasars is primarily due to compact and radio-faint systems (around the radio quiet–radio loud threshold). We show that our results rule out orientation as the origin for the differences between red and blue quasars and argue that they provide broad agreement with an evolutionary model.

**Key words:** galaxies: active – galaxies: evolution – galaxies: jets – quasars: general – quasars: supermassive black holes – infrared: galaxies – radio-continuum: galaxies.

## 1 INTRODUCTION

Quasars, often referred to as Quasi-Stellar Objects (QSOs), represent the most luminous subset of the overall population of Active Galactic Nuclei (AGN). Their prodigious output (bolometric luminosities up to  $10^{47} \text{ erg s}^{-1}$ ) is indicative of rapid accretion, at or near the Eddington limit, onto a supermassive black hole (BH;  $10^9 M_{\odot}$ ) that resides at the heart of the host galaxy. Quasars radiate across the electromagnetic spectrum, from radio to X-rays. The primary emission comes from the accretion onto the BH (in the form of an accretion disc) which produces thermal emission at ultraviolet (UV)–optical wavelengths. Surrounding the accretion disc is a geometrically and optically thick structure of cold molecular gas and dust (commonly referred to as the dusty “torus”) which obscures a direct view of the accretion disc from some viewing angles. The dust in the “torus” is heated by the accretion disc and emits thermally at mid-infrared wavelengths (MIR;  $5\text{--}40 \mu\text{m}$ ), dropping off steeply to the

far-infrared band (FIR;  $40\text{--}500 \mu\text{m}$ ; e.g. Elvis et al. 1994; Richards et al. 2006b; Netzer et al. 2007; Mullaney et al. 2011). In the radio waveband ( $>1 \text{ cm}$ ) emission produced by relativistic jets emerging from the vicinity of the black hole (BH) is sometimes detected; overall  $\approx 5\text{--}10\%$  of optically selected quasars are powerful in the radio waveband (e.g. Condon et al. 2013).

A standard spectroscopic signature of a quasar is the presence of broad emission lines superimposed onto a blue power-law continuum. However, the discovery of a subset of quasars with redder continuum emission (i.e., red optical/IR colours) has challenged the conventional view. Despite many studies in the literature (e.g. Rieke et al. 1982; Webster et al. 1995; Benn et al. 1998; Kim & Elvis 1999; Francis et al. 2000; Richards et al. 2003; Glikman et al. 2004, 2007, 2012; Urrutia et al. 2009; Banerji et al. 2012; Stern et al. 2012; Assef et al. 2013; Ross et al. 2015; LaMassa et al. 2016; Tsai & Hwang 2017; Kim & Im 2018), the nature of red quasars remains uncertain. The majority of studies ascribe the red colours as due to dust-reddening of the accretion-disc emission (e.g. Webster et al. 1995; Wilkes et al. 2002; Glikman et al. 2004,

\* lizelke.klindt@durham.ac.uk

2007; Rose et al. 2013; Kim & Im 2018). Nonetheless, depending on the selection and luminosity of the quasar, the red colours can also be due to (1) an excess of flux at longer wavelengths either from a red synchrotron component or the “contamination” of starlight from the host galaxy (e.g. Serjeant 1996; Benn et al. 1998; Francis et al. 2000; Whiting et al. 2001), or (2) an intrinsically red continuum due to differences in the accretion disc and/or Eddington ratio when compared to normal quasars (e.g. Richards et al. 2003; Young et al. 2008).

Ever since the first focused studies of red quasars over 20 years ago there has been debate over the relationship between red and blue quasars. If the red-blue quasar dichotomy is equivalent to that between nearby obscured and unobscured AGN then the different optical colours will be largely due to the orientation of an anisotropic obscuring structure (i.e., the dusty “torus”; e.g., Antonucci 1993; Urry & Padovani 1995). In this scenario red quasars will be more obscured by dust since they are viewed at inclinations closer to the equatorial plane of the dusty “torus” than blue quasars (i.e., a red quasar is simply an inclined blue quasar whereby the observed viewing angle intersects a larger column of dust).

Alternatively, a competing paradigm postulates that red and blue quasars are related within an evolutionary sequence that connects dust-obscured star formation (SF) with quasar activity through gas inflow and outflow/feedback (e.g., Sanders et al. 1988; Hopkins et al. 2008; Alexander & Hickox 2012). With this model the rare red quasar population represents a brief transitional phase (a few tens of Myr; Hopkins et al. 2008) between the dust-obscured SF and the blue quasar phase during which winds/jets drive away the obscuring dust, ultimately shutting down the SF and revealing an unobscured blue quasar.

Distinguishing between these competing scenarios is a major focus of red quasar studies. On the basis of emission line kinematics and X-ray analysis, some studies favour the orientation scenario to explain the nature of red quasars (e.g., Wilkes et al. 2002; Rose et al. 2013). Conversely, through a slew of different selection approaches (e.g., optical; near-infrared (NIR); radio) and multi-wavelength analyses, other studies have presented evidence that many red quasars show the properties expected for the brief evolutionary phase (e.g., Urrutia et al. 2008; Banerji et al. 2012, 2017; Glikman et al. 2012, 2015): major-merger driven gas inflows, dust-obscured SF, and energetic outflows. Irregardless of the fundamental nature of red quasars, all of these studies agree that the origin of the red quasar colours is due to the obscuration of a blue quasar continuum by dust; however, the location of the obscuring dust (i.e., in the nucleus versus the host galaxy) and its origin (i.e., a consequence of the inclination of the dusty “torus” versus the aftermath of a galaxy major merger event) remains uncertain.

A major challenge in comparing between different red quasar studies is the broad range of selection approaches adopted (e.g. Webster et al. 1995; Cutri et al. 2001; Gregg et al. 2002; Glikman et al. 2007; Banerji et al. 2012; Tsai & Hwang 2017); e.g., optical–NIR–MIR colour criteria; point-source morphologies; bright radio emission. Furthermore, most red quasar studies do not uniformly select a normal blue quasar sample to provide a reliable “control” to demonstrate that any observed differences (e.g., in redshift, lu-

minosity, BH mass, Eddington ratio) are specific to the red quasar population rather than being a consequence of the different selection approaches. To robustly demonstrate that there are fundamental differences between red and blue quasars which cannot be attributed just to orientation, the quasar samples must be selected in a uniform manner, carefully controlling for any additional selection effects.

In this work we have used the Sloan Digital Sky Survey (SDSS; York et al. 2000) to undertake a uniform selection of red and blue quasars to search for fundamental differences, and to hence distinguish between the evolutionary and orientation scenarios. In §2 we outline the multi-wavelength data we used to construct a quasar parent sample which is uniform in selection and unbiased in the radio waveband. We also define our red and blue quasar samples and constrain the amount of dust obscuration required to produce the optical colours of the red quasars. Based on our findings we construct luminosity-redshift matched subsamples which we use throughout the paper as a comparison to the full colour-selected quasar subsamples. In §3.1 we explore the radio properties of red and blue quasars and find that red quasars show an enhanced radio-detection fraction in comparison to blue quasars across all redshifts. In §3.2 we investigate the radio morphologies to determine which morphological structures are associated with the surfeit of radio-detected red quasars, and in §3.3 we explore the relation between the radio-detection fraction and the radio luminosity ( $L_{1.4\text{ GHz}}$  and  $L_{1.4\text{ GHz}}/L_{6\mu\text{m}}$ ) of red quasars. Overall we find a significant enhancement in the detection of compact and faint radio sources in the red quasar population, a result that becomes stronger towards radio-quiet quasars. These results strongly argue against a simple orientation model but are in broad agreement with an evolutionary model, which we discuss in §4. In this work we adopted a concordance flat  $\Lambda$ -cosmology with  $H_0 = 70\text{ km s}^{-1}\text{ Mpc}^{-1}$ ,  $\Omega_M = 0.3$ , and  $\Omega_\Lambda = 0.7$ .

## 2 DATA SETS AND QUASAR SAMPLE DEFINITION

In this study we explore the physical properties of red quasars at  $0.2 < z < 2.4$  to understand whether they are intrinsically different to the overall quasar population at the same epochs. The multi-wavelength data and catalogues we used to select red and blue quasars are highlighted in §2.1 and the details of our careful selection criteria are described in §2.2; Figure 1 presents a flowchart that summarizes the different steps that are taken in defining our full colour-selected subsamples. In §2.3 we utilise the MIR emission as a robust tracer of the nuclear power of quasars and define a  $L_{6\mu\text{m}}-z$  matched sample to minimise luminosity and redshift effects on our results.

### 2.1 Multi-wavelength data and catalogues

Our quasar selection is based on the SDSS DR7 Quasar Catalogue (Schneider et al. 2010). We utilise this catalogue in combination with MIR data from the Wide-field Infrared Survey Explorer (*WISE*; Wright et al. 2010) and radio data from the Faint Images of the Radio Sky at Twenty-Centimeters (FIRST; Becker et al. 1995, 2012; Helfand et al.

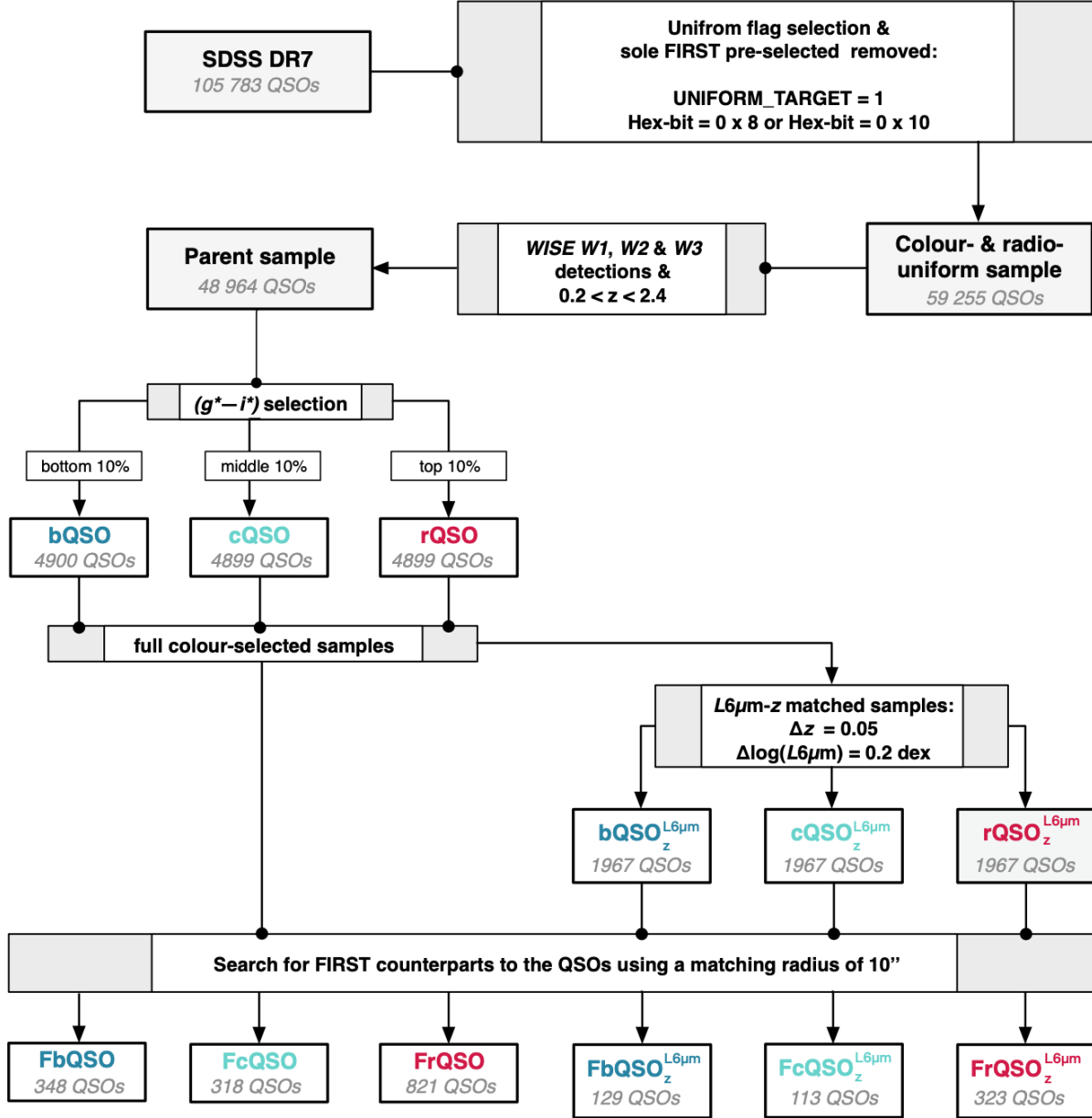


**Figure 1.** A schematic diagram of our selection process. We started with quasars from [Schneider et al. \(2010\)](#) and selected those with the uniform selection flag and excluded sources which were solely targeted for spectroscopic followup due to their FIRST pre-selection; i.e., sources which were selected only due to having a FIRST counterpart and did not satisfy any of the other selection criteria outlined in [Richards et al. \(2002\)](#). To construct a parent sample we included sources at redshifts of  $0.2 < z < 2.4$  with *WISE* detections in bands W1, W2 and W3 ( $\text{SNR} > 2$ ), and with bolometric luminosity and BH mass measurements in [Shen et al. \(2011\)](#). The parent sample was then equally subdivided into the bottom, middle and top 10% of the redshift dependent  $g^* - i^*$  distributions representing our full colour-selected samples termed as bQSOs, cQSOs and rQSOs, respectively (see [Figure 2](#)). Additionally, the bQSOs, cQSOs and rQSOs were matched in  $6\mu\text{m}$  luminosity and redshift to construct  $L_{6\mu\text{m}} - z$  matched colour-selected subsamples. Following the colour selection and luminosity-redshift matching, we searched for FIRST radio counterparts within a  $10''$  search radius; these samples represent FIRST-detected quasars termed as FbQSO, FcQSOs and FrQSOs for the FIRST-detected bQSOs, cQSOs and rQSOs, respectively. The source statistics for the different subsamples split into redshift bins are tabulated in [Table 1](#).

2015) and the NRAO VLA Sky Survey (NVSS; [Condon et al. 1998](#)) to refine our selection approach and quasar analyses.

### 2.1.1 Optical data: the SDSS DR7 Quasar Catalogue

The SDSS DR7 Quasar Catalogue ([Schneider et al. 2010](#), hereafter S10) consists of 105,783 spectroscopically confirmed quasars with luminosities of  $M_i < -22.0$  out to  $z = 5.48$  which exhibit at least one emission line with a full width at half-maximum (FWHM)  $> 1000 \text{ km s}^{-1}$  or ex-

hibit broad absorption line features. We briefly describe the construction of the quasar catalogue below.

The quasar selection algorithm described in Richards et al. (2002) was used to select primary candidate quasars for spectroscopic followup (see also Richards et al. 2001; Stoughton et al. 2002; Schneider et al. 2005; Vanden Berk et al. 2005). This algorithm distinguishes between quasars and the much more numerous stars and galaxies by (1) using their nonstellar colours obtained from the  $u^*$  (3543 Å),  $g^*$  (4770 Å),  $r^*$  (6231 Å),  $i^*$  (7625 Å) and  $z^*$  (9134 Å) broadband photometry and (2) searching for counterparts in the FIRST survey to all unresolved objects brighter than  $i_{\text{dered}}^* = 19.1$ .<sup>1</sup> The target colour selection is sensitive to red quasars (e.g., quasars with  $E(B - V) = 0.1$  have a high probability of being selected; see §2.2 of Richards et al. 2003), although the most reddened quasars will be missed. In addition, non-quasar selection algorithms were used to supplement the primary quasar selection, including (1) objects with ROSAT All-sky Survey (RASS, Voges et al. 1999, 2000) counterparts, (2) objects targeted as members of certain stellar populations (e.g.,  $F$  stars and Main-sequence turnoff stars) but whose spectra showed them to be quasars, and (3) serendipitous objects (FIRST matches or objects with peculiar colours; see Stoughton et al. 2002; Anderson et al. 2003; Vanden Berk et al. 2005; Richards et al. 2006a; Shen et al. 2007; Schneider et al. 2010; Shen et al. 2011, for further details on the SDSS selection algorithms). These candidates were only assigned fibres once the main samples of galaxies, Luminous Red Galaxies (LRGs) and quasars were tiled. Hence, these samples are incomplete and in combination with the inclusion of the “Special Plates” in the Galactic cap (e.g., Stripe 82 Stoughton et al. 2002; Adelman-McCarthy et al. 2006), were designed to explore the limits of the primary selection algorithm, to go deeper and to target objects with atypical colours.

The selection of quasars via earlier versions of the algorithm or from the Special Plates introduced a non-uniformity in the selection of the S10 quasar sample and, therefore, approximately half of these objects are not suitable for statistical analyses (Shen et al. 2011; Kratzer & Richards 2015; Park et al. 2015). However, S10 identify targets that satisfy *a posteriori* the Richards et al. (2002) selection algorithm, indicated with the uniform flag (UNIFORM.TARGET = 1; see Shen et al. 2011; Park et al. 2015; Kratzer & Richards 2015), which provides a statistically reliable sample of 59,514 quasars up to  $z = 5.48$ . Of these, only 259 quasars were targeted uniquely by FIRST pre-selection.

### 2.1.2 Radio data: searching for FIRST counterparts

The VLA Faint Images of the Radio Sky at Twenty-Centimeters (FIRST; Becker et al. 1995, 2012; Helfand et al. 2015) is a 1.4 GHz radio survey that observed  $\approx 10,000$  deg<sup>2</sup> of the SDSS region at a spatial resolution of 5". The  $5\sigma$  source detection threshold of 1 mJy makes it beneficial to detect quasars down to low radio luminosities; i.e., including even radio-quiet AGN. The FIRST survey comprises 946,432

radio sources of which 30% have a spectroscopic SDSS counterpart (e.g., Ivezić et al. 2002).

When cross-matching between different surveys there is a trade-off between completeness and the number of false associations. Since the majority of the SDSS quasars are likely to be unresolved in FIRST, a high completeness and low random association can be achieved even when adopting a small search radius. Based on the analysis of Lu et al. (2007), we adopted a 10" cross-matching radius. They showed that the false association rate within 10" of the QSO position is only 0.2%, with just 2% of radio quasars in SDSS having radio structures that extend beyond 10" and have an undetected radio core in FIRST. Therefore, we consider all FIRST radio sources with centroidal positions within 10" of the quasar to be directly associated, and summed their integrated flux. In practice only 6% of all our radio-detected quasars have multiple FIRST counterparts treated in this fashion (see §3.2). To explore our incompleteness to large radio sources we used additional data from the NVSS (Condon et al. 1998) which has a beam size of 45", significantly larger than FIRST and our cross-match radius (§3.2).

We calculated the 1.4 GHz luminosities using the methodology described in Alexander et al. (2003), assuming a uniform radio spectral index of  $\alpha = 0.5$  to compute a K-correction (which is the division between steep and flat radio spectrum quasars; e.g., Wall 1975; Kimball & Ivezić 2008).<sup>2</sup> In this work we used the FIRST integrated flux ( $F_{\text{int}}$ ) to compute the radio luminosities and the FIRST peak flux ( $F_{\text{peak}}$ ) to establish whether a source is radio faint (i.e.,  $F_{\text{peak}} < 3$  mJy).

### 2.1.3 Infrared data: searching for WISE counterparts

To explore the dust properties of red quasars in comparison to blue quasars, we searched for MIR counterparts from the Wide-field Infrared Survey Explorer (WISE; Wright et al. 2010) which mapped the entire sky in four bands: W1 ( $\lambda = 3.4 \mu\text{m}$ ;  $PSF = 6.1''$ ), W2 ( $\lambda = 4.6 \mu\text{m}$ ;  $PSF = 6.4''$ ), W3 ( $\lambda = 12 \mu\text{m}$ ;  $PSF = 6.5''$ ) and W4 ( $\lambda = 22 \mu\text{m}$ ;  $PSF = 12.0''$ ). Using the Query Engine from the Infrared Science Archive at NASA/IPAC we matched the uniformly selected S10 quasars to the All-Sky WISE Source Catalogue (ALLWISE) within a 2.7" radius. This ensured a 99.5% certainty that the optical source is matched to the correct MIR counterpart (Lake et al. 2012). We found a WISE counterpart for 58,137 uniformly selected S10 quasars.

Since the MIR emission is a robust tracer of the reprocessed accretion disc emission from dust that is free of the effects of extinction, we determined the intrinsic luminosities of the quasars on the basis of the MIR fluxes after ensuring that the MIR emission is not significantly contaminated by non-AGN processes (see §2.3.1). We computed the rest-frame  $6\mu\text{m}$  luminosity ( $L_{6\mu\text{m}}$ ) by log-linear interpolation or extrapolation of the fluxes in the W2 and W3 bands, assuming that they are equivalent to monochromatic fluxes at the effective wavelength of the filters.

<sup>1</sup> Hereafter all SDSS PSF magnitudes used in this paper refer to the Galactic-extinction corrected magnitudes provided in Shen et al. (2011).

<sup>2</sup> We define the spectral index  $\alpha$  as  $f_\nu \propto \nu^{-\alpha}$ .

## 2.2 Distinguishing between red and blue quasars: full colour-selected samples

A variety of different approaches have been adopted in the literature to select red quasars which makes it difficult to draw conclusions about their properties with respect to blue quasars. Our main aim is to construct a carefully controlled and redshift-sensitive experiment in which both red and blue quasars are drawn from the same parent sample to allow for a systematic exploration of their multi-wavelength properties. In §2.2.1 we construct a parent sample using the aforementioned catalogues/surveys and in §2.2.2 we define our red and blue quasar samples, referred to here as our full colour-selected samples.

### 2.2.1 Defining the quasar parent sample

As mentioned in §2.1.1, the SDSS quasar selection approach is complex which introduces some non-uniformity in the overall quasar sample. We therefore sought a selection approach which is uniform and minimises radio biases introduced by the FIRST pre-selection of SDSS quasars.

Figure 1 shows a flowchart that summarizes the different steps we took in defining our parent sample to then select red and blue quasars (§2.2.2); the source statistics in each sample are reported in Table 1. To construct a uniform parent sample we, firstly, selected S10 quasars with the uniform flag and then, using the hexadecimal bit value of the ‘BEST’ flag (see Stoughton et al. 2002; Schneider et al. 2010), we identified and removed sources pre-selected solely on the basis of their FIRST detection (BESTFLAG =  $0 \times 8$  for sources at high Galactic latitude and BESTFLAG =  $0 \times 10$  for sources at low Galactic latitude).

In addition to uniform selection, our sample is restricted to the redshift range  $0.2 < z < 2.4$  and required a SNR  $> 2$  in the *WISE* W1, W2, and W3 bands to allow the estimation of  $L_{6\mu\text{m}}$ . We excluded 70 sources of the uniform sample which lacked bolometric luminosity measurements. This yielded a final parent sample of 48,964 quasars that are uniform in selection and unbiased in the radio waveband within our selected redshift range.

### 2.2.2 Defining the full colour-selected samples

To distinguish between red and blue quasars we produced  $g^* - i^*$  colour distributions of our uniformly selected parent sample (§2.1.3) as a function of redshift. We define red quasars (rQSOs) and blue quasars (bQSOs) by selecting the respective reddest 10% and the bluest 10% of the colour distribution. Additionally we selected the 10% of quasars around the median of the  $g^* - i^*$  distribution to construct a control sample (cQSOs). Hereafter we refer to all non-red quasars (including the bQSO and cQSO subsamples) as blue quasars.

In Figure 2 we illustrate the selection of the three colour-selected quasar samples. In order to construct a rQSO selection which is sensitive to the redshift evolution of quasar SEDs we sorted the quasars by redshift and constructed the  $g^* - i^*$  distributions in contiguous redshift bins consisting of 1000 sources as shown in the zoom-in panel in Figure 2. We restricted our analysis to  $z \leq 2.4$  due to the low optical completeness of quasars in S10 at  $2.5 < z < 3.0$ . This is a

**Table 1.** Source statistics for the quasar samples in four different redshift bins. We present the number of sources for the uniformly selected parent sample, the full colour-selected samples (bQSOs, cQSOs and rQSOs), the  $L_{6\mu\text{m}} - z$  matched colour samples (bQSO $_z^{L_{6\mu\text{m}}}$ , cQSO $_z^{L_{6\mu\text{m}}}$  and rQSO $_z^{L_{6\mu\text{m}}}$ ) and their respective FIRST-detected subsamples.

Sample	$N_{z1-z4}$	$N_{z1}$	$N_{z2}$	$N_{z3}$	$N_{z4}$
(1)	(2)	(3)	(4)	(5)	(6)
Parent	48,964	5,402	6,021	18,286	19,255
Colour-selected QSO samples					
bQSOs	4,900	535	613	1,822	1,923
cQSOs	4,899	543	597	1,826	1,929
rQSOs	4,899	545	590	1,833	1,930
FbQSOs	348	62	71	110	105
FcQSOs	318	52	48	121	97
FrQSOs	821	99	127	298	297
Matched $L_{6\mu\text{m}} - z$ QSO samples					
bQSO $_z^{L_{6\mu\text{m}}}$	1,967	159	256	781	771
cQSO $_z^{L_{6\mu\text{m}}}$	1,967	161	252	780	773
rQSO $_z^{L_{6\mu\text{m}}}$	1,967	161	252	781	772
FbQSO $_z^{L_{6\mu\text{m}}}$	129	12	32	44	41
FcQSO $_z^{L_{6\mu\text{m}}}$	113	13	20	43	37
FrQSO $_z^{L_{6\mu\text{m}}}$	323	39	51	121	112

**Notes.** (1): Target samples used in this study: Parent QSOs represents the uniformly selected S10 quasars with W1 – W3 detections, b-, c-, rQSOs are the  $g^* - i^*$  colour-selected samples and F-b-, c-, rQSOs are the radio-bright quasars matched to FIRST (see Figure 2). (2)–(6): Source statistics for each sample within the respective redshift bins; i.e., across the full  $z$  range in our study,  $0.2 < z_1 < 0.5$ ,  $0.5 < z_2 < 0.8$ ,  $0.8 < z_3 < 1.5$  and  $1.5 < z_4 < 2.4$ .

consequence of the crossing between the stellar and quasar loci in the SDSS multicolour space (see e.g., Richards et al. 2002). Even though the  $u^* - z^*$  colour provides the broadest wavelength baseline for colour separation, the SDSS photometry in both of these bands is shallow and is more affected by atmospheric attenuation (e.g., Ivezić et al. 2002). Furthermore, the  $u^*$ -band is heavily affected by the Lyman break at  $z \geq 1.9$  which motivates our use of the  $g^*$ -band (only influenced at higher redshifts, i.e.,  $z \geq 2.5$ ).

Therefore, the  $g^* - i^*$  colour was used to select red and blue quasars with the broadest possible wavelength range while optimising photometric depth (see e.g., Richards et al. 2003). To verify that our colour selection does indeed reliably identify quasars with red and blue colours, and is not strongly influenced by broad emission line contamination in the  $g^*$  or  $i^*$  bands, we compared the  $g^* - i^*$  to  $u^* - r^*$  colours of the bQSOs, cQSOs and rQSOs as shown in Figure 3. We note that the rQSOs selected using  $g^* - i^*$  are also red in  $u^* - r^*$  when comparing to the bQSOs and cQSOs. Approximately 2% of the cQSOs have  $g^* - i^* > 0.5$  (all of these sources are

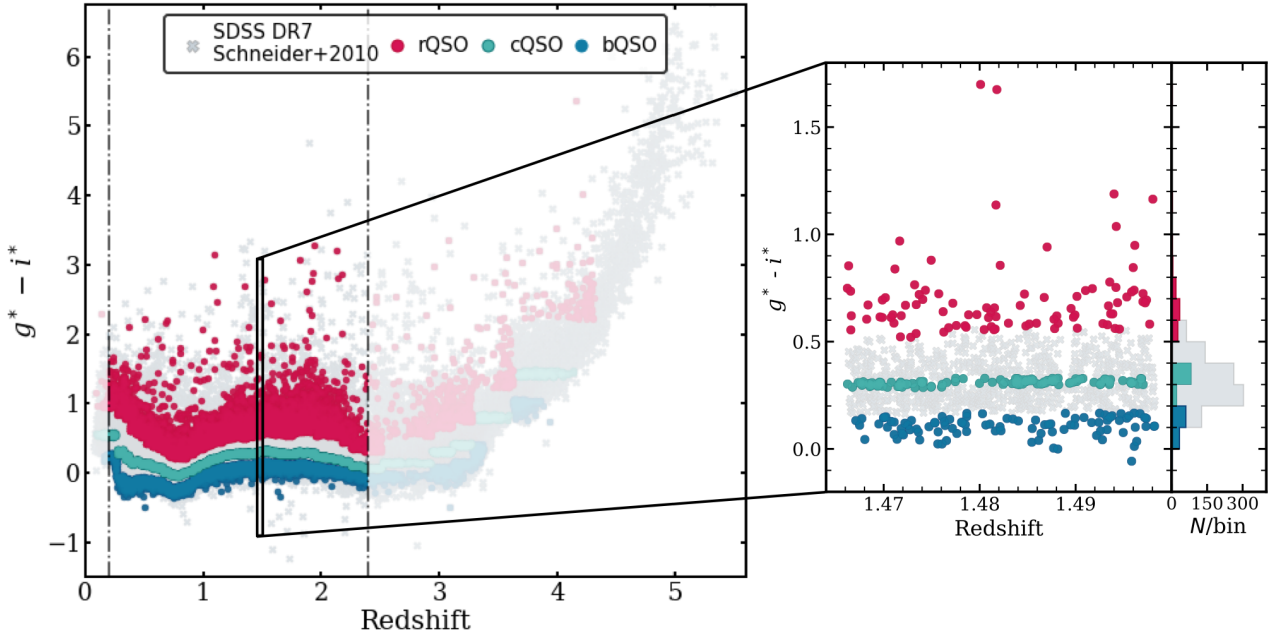


**Figure 2.** The  $g^* - i^*$  colours versus redshift for the bQSOs (blue circles), cQSOs (green circles) and rQSOs (red circles) explored in this study. Our selected quasars are superimposed on the distribution of S10 (grey; Schneider et al. 2010). Also indicated is the redshift range of our study ( $z = 0.2 - 2.4$ ; dash-dot black line). *Zoom-in panel:* An illustration of the selection of the bQSOs (bottom 10%), cQSOs (middle 10%) and rQSOs (top 10%) using the  $g^* - i^*$  colours and redshift for an example bin of 1000 sources. The  $g^* - i^*$  distribution is shown on the right.

at  $z < 0.3$ ; see Figure 2). However, this is not a failure of our quasar selection approach and is a natural consequence of our redshift-sensitive selection technique. Overall, within the full colour-selected sample there are  $\approx 4900$  quasars in each of the bQSO, cQSO, and rQSO sub samples, of which 348, 318, and 821 are radio detected, respectively.

### 2.2.3 Dust extinction in red quasars

The most common explanation for the optical colours of red quasars is dust extinction, whether due to the inclination of a dusty torus resulting from an increase in dust along the line-of-sight or an obscuring dust envelope in which the young red quasar is embedded. We note that, due to the optical selection criteria, the SDSS will miss the most reddened quasars both because of their colours (red quasars overlay the stellar locus in most SDSS colour-colour diagrams) and because of the optical survey flux limit (e.g., Glikman et al. 2004; Banerji et al. 2012, use NIR data and select SDSS optical drop outs to define their red quasar samples).

In Figure 4 we visually examine the amount of dust reddening implied by our selection technique by plotting the  $\Delta(g^* - i^*)$  colour as a function of redshift for the bQSOs, cQSOs and rQSOs. The dashed lines denote the effect of SMC-type extinction (Prevot et al. 1984) as a function of redshift with  $E(B - V) = 0.04, 0.12$  and  $0.2$  (e.g., Richards et al. 2003) on the emission of a typical quasar. Our selection of red quasars is broadly consistent with  $E(B - V) > 0.04$  at  $z > 0.8$  for a blue quasar SED. This corresponds to an equivalent hydrogen column density of  $N_{\text{H}} > 2.8 \times 10^{20} \text{ cm}^{-2}$  assuming an SMC-like dust-to-gas ( $E(B - V)/N_{\text{H}}$ ) ratio, comparable to that found towards the HII-regions in normal

galaxies (Buchner et al. 2017); we note that LaMassa et al. (2016) and Glikman et al. (2017) find that radio-selected red quasars have dust-to-gas ratios up-to an order of magnitude below the Galactic value, which would lead to higher hydrogen column densities by up-to an order of magnitude. The range in  $\Delta(g^* - i^*)$  colours suggest that the majority of our rQSOs require  $A_{\text{V}} \sim 0.1 - 0.5$  mag to produce the observed optical colours. By comparison, NIR based selection techniques are sensitive to selecting red quasars with a dust extinction of up to  $A_{\text{V}} \sim 1 - 6$  mag (e.g. Glikman et al. 2004; Banerji et al. 2012), hence the rQSOs in our study represent less extreme dust-reddened red quasars.

### 2.3 Defining the AGN power at rest-frame $6 \mu\text{m}$ : luminosity-redshift matched samples

To reliably infer any fundamental differences in the properties of the rQSOs from blue quasars (i.e., the bQSOs and cQSOs) we must ensure that our results are not driven by differences in the bolometric luminosities of the quasars. Shen et al. (2011) provide bolometric luminosities ( $L_{\text{bol}}$ ) for the S10 quasar sample, however, they are inferred from rest-frame UV-optical continuum measurements and have not been corrected for dust extinction. Consequently, the  $L_{\text{bol}}$  values are likely to be significantly underestimated in the rQSOs, which will also lead to unreliable BH masses and Eddington ratios. We therefore calculate the bolometric luminosities for our quasar subsamples using the MIR *WISE* data, as described below, and utilise these to create luminosity-redshift matched samples.

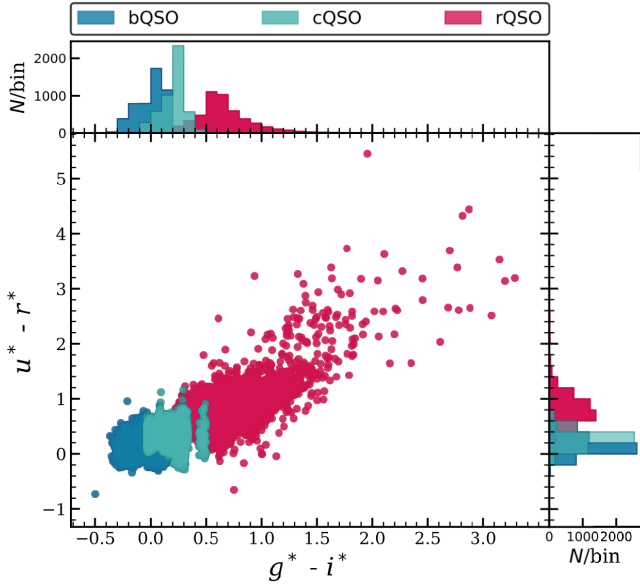


**Figure 3.** A colour-colour diagram of the  $u^* - r^*$  vs.  $g^* - i^*$  colours for the full colour-selected samples; the bQSOs, cQSOs and rQSOs are indicated using the colour scheme in Figure 2 for redshifts in the range  $0.2 < z < 2.4$ . It is evident that the colours of red quasars are more broadly distributed in the colour-colour parameter space than more blue quasars, even in bands unrelated to our red quasar selection approach. Furthermore, our  $g^* - i^*$  colour selection appears to be broadly consistent with other optical colours in selecting quasars, e.g.,  $u^* - r^*$ . A minority of the cQSOs have  $g^* - i^* > 0.5$  which is not a failure of our approach but a normal consequence of our redshift-sensitive selection technique; see also Figure 2 where this is evident for quasars at  $z < 0.3$ .

### 2.3.1 MIR measurements: a more robust approach

In order to accurately quantify the MIR emission from the quasar, it is imperative to verify that it is not contaminated by the host galaxy. Since the dusty AGN torus radiates predominantly at MIR wavelengths while star formation from the host galaxy peaks at FIR wavelengths, we would expect the MIR emission from our quasars to be dominated by the AGN. To verify this, we make use of the diagnostic *WISE* three-band colour-colour diagram on which Mateos et al. (2012) define a region (called the “AGN wedge”; Figure 5) which identifies AGN with red MIR power-law SEDs with a spectral index  $\alpha \leq -0.3$ . Host star-formation with a MIR luminosity  $> 10\%$  of that of the AGN would systematically move QSOs out of the lower right of the wedge; however, this requires high star formation rate (SFR) levels (e.g.,  $> 100 M_{\odot}/\text{yr}$  at  $z > 1$ ).

In Figure 5 we plot the *WISE* colours ( $W1 - W2$  vs  $W2 - W3$ ) of our colour-selected quasars and indicate the AGN wedge to show where AGN are expected to lie. The bulk ( $\sim 95\text{--}99\%$ ) of the quasars lie within the wedge; however, a small fraction lie outside as reported in Table 2. Most of the bQSO and cQSO outliers are higher redshift sources ( $z > 1.5$ ), while the majority of the rQSO outliers tend to be at lower redshifts ( $z < 1.5$ ); the same result is found for the FIRST-detected samples. The colours of the sources outside of the wedge at low redshifts can potentially be attributed to dominant host galaxy emission in low-luminosity

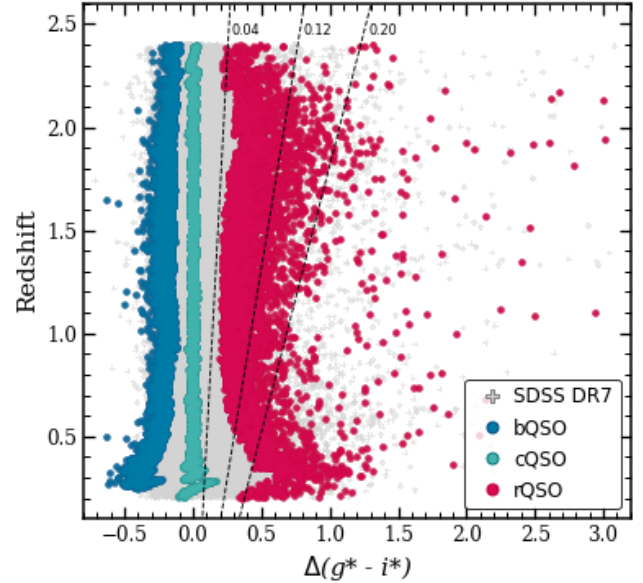


**Figure 4.** Redshift vs.  $\Delta(g^* - i^*)$  for the bQSOs, cQSOs and rQSOs using the colour scheme in Figure 2. We illustrate the relative colours for our parent sample as well (faded grey points). The dashed lines are the dust-reddening for  $E(B - V) = 0.04, 0.12$  and  $0.2$  (Richards et al. 2003), which correspond to  $A_V = 0.1, 0.3,$  and  $0.5$  mags for a typical quasar SED. The range in the relative colours of the rQSOs suggests that the majority require  $A_V \sim 0.1 - 0.5$  mag to produce the observed optical colours.

**Table 2.** The percentage of bQSOs, cQSOs and rQSOs which lie outside the Mateos et al. (2012) AGN wedge across  $0.2 < z < 2.4$ . Tabulated are both the colour-selected SDSS samples, as well as the FIRST-detected QSOs.

Sample	Nu. outside	Percentage outside		
		$0.2 < z < 2.4$	$z < 1.5$	$z > 1.5$
Colour-selected quasars				
bQSO	56	1%	0.3%	0.8%
cQSO	82	2%	0.8%	0.9%
rQSO	305	6%	4%	2%
FIRST-detected quasars				
FbQSO	8	2%	0.9%	1%
FcQSO	9	3%	1%	2%
FrQSO	43	5%	3%	2%

quasars. However, since only a small fraction of the quasars lie outside of the AGN wedge we can confidently assert that  $> 90\%$  of the MIR light in most of our quasars come from an AGN, and for these, we can reliably estimate their MIR AGN luminosities ( $L_{6\mu\text{m}}$ ; see §2.1.3 for the details of the luminosity calculation).

In Figure 6 we plot the  $L_{6\mu\text{m}}$  as a function of redshift. The median  $\log(L_{6\mu\text{m}})$  of the colour-selected (square) and FIRST-detected (cross) quasars are also plotted in the respective  $z$ -bins. We find lower median  $\log(L_{6\mu\text{m}})$  values for the rQSOs than the bQSOs at low redshifts ( $z < 0.8$ ). This is also mirrored in the higher fraction of rQSO outliers in the AGN wedge at these redshifts and may be the consequence of host-galaxy dilution affecting the colours of the lower luminosity quasars at lower redshifts. However, at higher red-

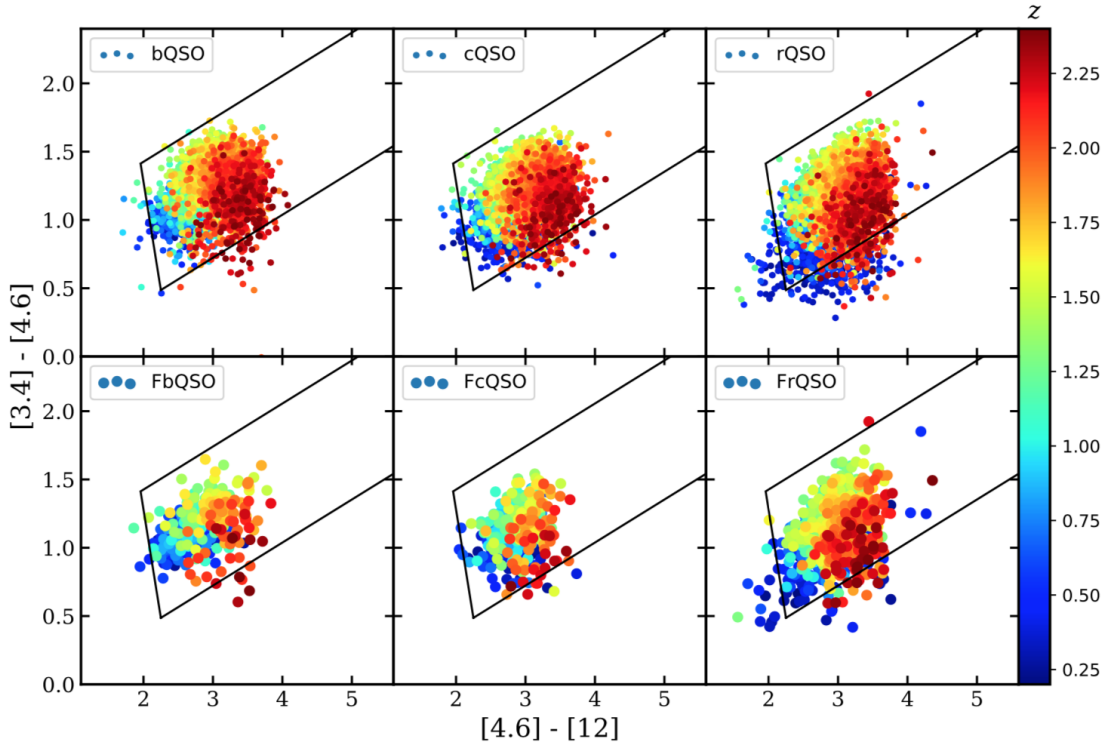


**Figure 5.** A *WISE* colour-colour diagram for our optically selected quasars colour coded by redshift. The [Mateos et al. \(2012\)](#) AGN wedge is indicated with black solid lines. The bQSOs, cQSOs and rQSOs are shown in the top panels from left to right, and the radio-detected FbQSOs, FcQSOs and FrQSOs are presented in the bottom panels from left to right, respectively. The majority of the quasars lie in the AGN wedge; see [Table 2](#).

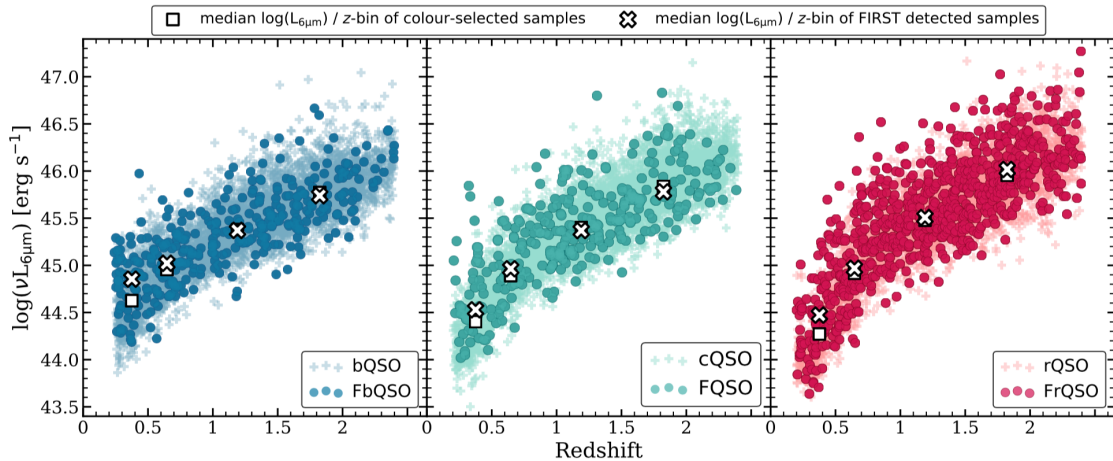


**Figure 6.** Rest-frame  $6\mu\text{m}$  luminosity versus redshift for the bQSO, cQSO and rQSO quasars with the radio-detected FbQSOs, FcQSOs and FrQSOs overlaid. The median values for full colour-selected samples (X's) and FIRST-detected samples (squares) in each redshift bin are also plotted.

shifts ( $0.8 < z < 2.4$ ) the opposite trend is seen where the rQSOs peak at higher  $6\mu\text{m}$  luminosities in comparison to the bQSOs and cQSOs (both in terms of higher median luminosities and larger maximum values). These effects could be a consequence of the optical selection of SDSS quasars which would mean that rQSOs that are obscured in the optical/UV by dust will only satisfy the SDSS quasar selection if they are intrinsically more luminous.

If the rQSOs are more subject to dust extinction, then

we would expect the optical AGN emission to be relatively weaker when compared to the  $L_{6\mu\text{m}}$  than the bQSOs and cQSOs. In [Figure 7](#) this is demonstrated by a comparison between the inferred bolometric luminosities from [Shen et al. \(2011\)](#) ( $L_{\text{bol,Shen}}$ ) to those derived from the  $6\mu\text{m}$  luminosity:  $L_{\text{bol,6}\mu\text{m}} = BC_{6\mu\text{m}} \times L_{6\mu\text{m}}$ , where we adopted  $BC_{6\mu\text{m}} = 8$  from [Stanley et al. \(2015\)](#). The continuum luminosities at rest-frame  $5100\text{ \AA}$  (left),  $3000\text{ \AA}$  (middle) and  $1350\text{ \AA}$  (right) provided in [Shen et al. \(2011\)](#) were used as the optical bolo-



metric luminosity. The median luminosity ratios (vertical dash-dot lines) computed from the 5100 Å luminosity are relatively consistent for the bQSOs, cQSOs and rQSOs. Contrariwise, as we approach shorter wavelengths, going from 3000 Å to 1350 Å luminosities, the median luminosity ratios of the red quasars decrease with respect to that of the blue quasars. This is the signature that we would expect for dust reddening as the shorter wavelength emission will be more suppressed for a fixed amount of obscuration than longer wavelength emission. Conversely to the underestimated luminosities, a few red quasars have notable overestimated optical bolometric luminosities (lower tail) which may be due to host contamination in lower luminosity quasars at low redshifts. At  $z < 0.5$  the  $\Delta(g^* - i^*)$  values of the blue and red quasars are seen to deviate from the overall population (see Figure 4); the blue quasars have bluer colours than the median quasar at the specific redshift, whereas the red quasars have redder colours. A possible explanation for the change in the apparent shape of the distribution is likely host galaxy contamination at lower redshifts.

### 2.3.2 Defining the luminosity-redshift matched colour-selected quasar samples

The different optical and MIR luminosity distributions between the bQSOs, cQSOs and rQSOs shown in §2.3.1 could skew any differences in the intrinsic properties between red and blue quasars. We have therefore adopted a luminosity and redshift matching approach to refine our quasar samples and exclude any biases in our results introduced by luminosity differences.

We luminosity matched the bQSOs, cQSOs and rQSOs in rest-frame 6 μm luminosity and redshift using tolerances of 0.2 dex and 0.05, respectively, with the following procedure (see Figure 1 and Table 1): (1) we used the 2-d Cartesian Anisotropic algorithm from the ‘Triple Match’ function in TOPCAT (Taylor 2005, 2006) keeping the best symmetric matches of the bQSOs, cQSOs and rQSOs in  $L_{6\mu\text{m}}$  and redshift (bQSO $_z^{L_{6\mu\text{m}}}$ , cQSO $_z^{L_{6\mu\text{m}}}$  and rQSO $_z^{L_{6\mu\text{m}}}$ ) and (2) we associated the quasars in these matched samples to FIRST within a 10'' radius (FbQSO $_z^{L_{6\mu\text{m}}}$ , FcQSO $_z^{L_{6\mu\text{m}}}$  and FrQSO $_z^{L_{6\mu\text{m}}}$ ), as described in §2.1.2. Overall, within the  $L_{6\mu\text{m}} - z$  matched colour-selected sample there are 1967 quasars in each of the bQSO, cQSO, and rQSO sub samples, of which 129, 113, and 323 are radio detected, respectively.

## 3 RESULTS

In this section we use our two defined samples (the full colour-selected sample and the  $L_{6\mu\text{m}} - z$  matched colour-selected sample) to search for fundamental differences between the radio properties of red and blue quasars. We explore the radio-detection rates in §3.1, the radio morphologies in §3.2, and the radio luminosities ( $L_{1.4\text{GHz}}/L_{6\mu\text{m}}$ ) in §3.3.

**Table 3.** The percentage of bQSOs, cQSOs, and rQSOs detected with FIRST. We also report the the detection fraction for non-red quasars; i.e., excluding the 10% of the  $g^* - i^*$  distribution. Also given are the  $1\sigma$  uncertainties on the radio-detection fractions obtained from Bayesian statistics. See Table 1 for the source statistics of each sample in the respective redshift ranges and the sample descriptions.

Redshift	FIRST-detected percentage (%)			
	bQSO	cQSO	rQSO	non-red QSO
$0.2 < z < 0.5$	$11.6^{+1.5}_{-1.2}$	$9.6^{+1.4}_{-1.1}$	$18.2^{+1.8}_{-1.5}$	$7.1^{+0.4}_{-0.3}$
$0.5 < z < 0.8$	$11.6^{+1.4}_{-1.2}$	$8.0^{+1.3}_{-0.9}$	$21.5^{+1.8}_{-1.6}$	$6.7^{+0.2}_{-0.2}$
$0.8 < z < 1.5$	$6.0^{+0.6}_{-0.5}$	$6.6^{+0.6}_{-0.5}$	$16.3^{+0.9}_{-0.8}$	$5.0^{+0.2}_{-0.2}$
$1.5 < z < 2.4$	$5.5^{+0.6}_{-0.5}$	$5.0^{+0.5}_{-0.5}$	$15.4^{+0.8}_{-0.8}$	$7.6^{+0.4}_{-0.4}$

### 3.1 FIRST detection rates of red versus blue quasars

The FIRST radio-detection rate as a function of the median redshift in each of the four redshift bins for the colour-selected samples is presented in Figure 8. We used the Bayesian binomial confidence interval technique discussed in Cameron (2011) to calculate  $1\sigma$  uncertainties on the radio-detection fractions for both the full and  $L_{6\mu\text{m}} - z$  matched colour-selected samples. In Table 3 we show the source statistics for the different samples.

The bQSOs and cQSOs have similar radio-detection fractions of  $\approx 5\% - 10\%$  across all redshifts. However, it is apparent that rQSOs always exhibit a significantly higher FIRST detection rate ( $\approx 15\% - 20\%$ ) relative to non-red quasars; i.e., the radio-detection fraction of red quasars is a factor of  $\approx 2 - 3$  times larger than blue quasars. This enhancement is also apparent if we compute the radio-detection fraction for non-red quasars in our sample; i.e., all quasars in the  $g^* - i^*$  colour distribution excluding the reddest 10%. The FIRST detection rates for these quasars are consistent with those of the bQSOs and cQSOs and, hence, they represent the typical quasar population of which only 5–10% are radio bright. Our results are consistent between the full and  $L_{6\mu\text{m}} - z$  matched colour-selected samples.

In our colour sample definitions we have taken the top 10% to define rQSOs (see §2.2). In Figure 9 we show how the radio-detection fraction changes from the bluest to reddest quasars: the top 10% of the reddest SDSS quasars always show the largest radio-detection fraction; however, we note that a more refined colour-based selection of red quasars could result in even more significant differences from blue quasars.

### 3.2 Radio morphologies of red versus blue quasars

Given the differences in the radio-detection fractions of red and blue quasars it is useful to determine whether there are associated differences in the radio morphologies; i.e., whether red quasars favour a specific radio morphological class above another. Radio-detected quasars often exhibit large scale radio jets and lobes which extend to tens of kpc, and in extreme cases can reach up to several Mpc (e.g., Muxlow & Garrington 1991). Their radio morphologies are

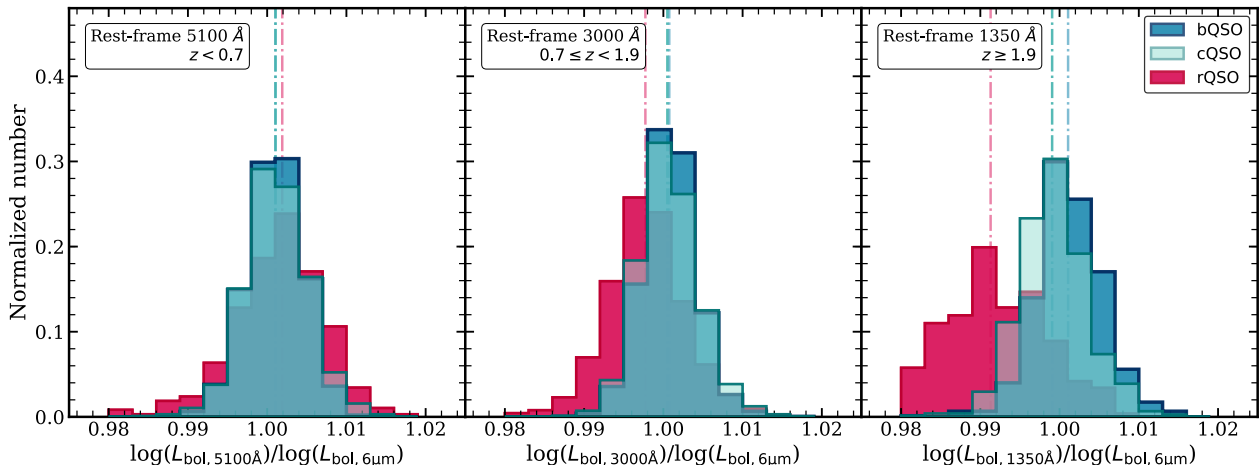


**Figure 7.** Luminosity ratio distributions using the continuum luminosities at rest-frame 5100 Å (left, BC = 9.26), 3000 Å (middle, BC = 5.15) and 1350 Å (right, BC = 3.81) adopted from Shen et al. (2011) and the inferred bolometric luminosity from the rest-frame 6  $\mu$ m luminosity with a bolometric correction of BC = 8. The vertical dash-dot lines illustrate the median luminosity ratio for the respective radio-detected quasar subsamples.

diverse but can be broadly characterised into two groups: core and extended radio sources (e.g., Peterson 1997; Lu et al. 2007). Core radio sources are spatially unresolved at resolutions similar to FIRST and tend to have flat radio spectra ( $\alpha < 0.5$ ). In contrast, quasars with extended radio morphologies have radio spectra that are steep ( $\alpha > 0.5$ ) and generally have the signature of two symmetric lobes (spatially resolved), although they can exhibit asymmetric lobes, jet-tail structures and other extended features. Extended radio sources are further differentiated into two main classes based on the surface brightness of the core to lobes, i.e., Fanaroff-Riley (FR) type I and II (Fanaroff & Riley 1974), where the former are core-dominated systems and the latter are lobe-dominated systems (e.g., Fanaroff & Riley 1974; Bicknell 1995).

With the modest resolution of FIRST we can explore radio morphologies for sources that extend beyond the 5'' beam size of the survey (this corresponds to projected sizes in the range 17–41 kpc at  $z = 0.2 - 2.4$  for our assumed cosmology). However, given the diverse range of radio morphologies of quasars, some will be too extended to be picked up by FIRST. Given these challenges we developed a comprehensive strategy to identify potentially extended radio sources, which we then visually classify using a simple approach that captures the morphological diversity of radio-detected quasars. Our approach to identify and classify potentially extended sources is illustrated in Figure 10 and is described below.

The FIRST survey decomposes radio sources into multiple gaussian components and reports size measurements for these components (White et al. 1997). Therefore the simplest approach in identifying extended sources is to search for cases where the gaussian sizes are larger than the FIRST beam size (5'') or with multiple radio counterparts within our cross-match radius of 10''.<sup>3</sup> This approach will identify

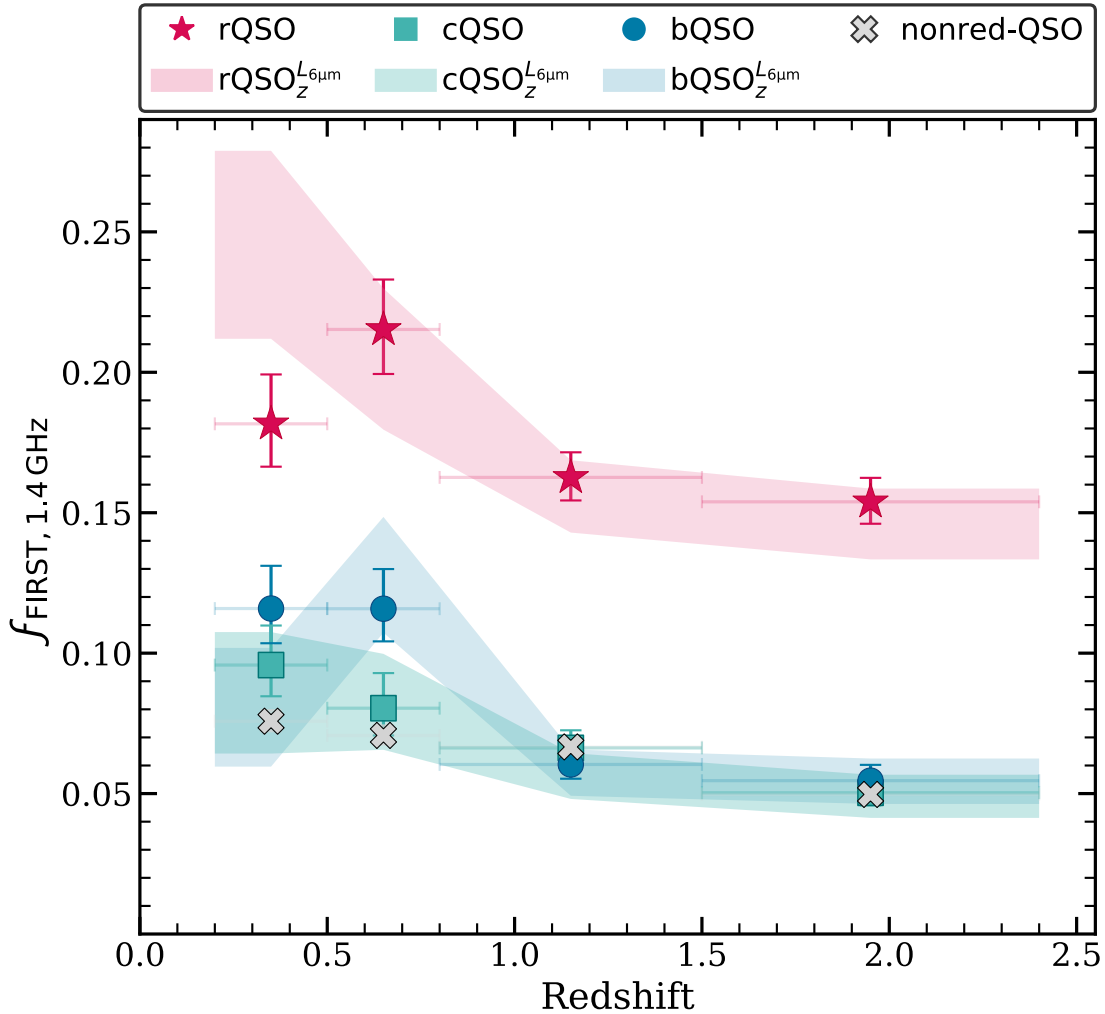
the vast majority of extended sources but will miss the most extended systems that lack bright radio cores; i.e., sources with very large lobe structures that lie beyond our 10'' cross-match radius and remain undetected by FIRST due to a faint radio core. To overcome this limitation we employed the 1.4 GHz NVSS survey which overlaps with the FIRST and SDSS footprint, but has a beam size of 45'', significantly larger than FIRST. This allows for the inclusion of large-scale radio structures beyond 10''. Using the methodology given in Lu et al. (2007), we estimate that only  $\approx 0.2\%$  will have spurious matches or unassociated sources for  $r = 10''$  (this increases to  $\approx 4\%$  for  $r = 45''$ ). We note that since NVSS is 2.5 times less sensitive than FIRST, faint diffuse extended sources will be missed in this analysis.

Figure 11 shows the NVSS versus FIRST fluxes for the FbQSOs, FcQSOs and FrQSOs. The majority of the sources follow a 1:1 trend. In this figure sources indicated with crosses have NVSS fluxes that are at least twice their FIRST fluxes: 12%, 10% and 7% of the FbQSOs, FcQSOs and FrQSOs are highlighted. For these sources FIRST may have underestimated their extended emission and they were visually assessed (see Figure 10). While radio variability may also explain these single component outliers (e.g., Heeschen et al. 1987; Kraus et al. 2003; Barvainis et al. 2005; Czerny et al. 2008), we nevertheless include them as potential extended sources.

All potentially extended sources highlighted by the process illustrated in Figure 10 were visually classified by three people (LK, DMA, DJR) using cutout images at 1.4 GHz extracted from the VLA FIRST server. Overall we inspected 396 FIRST cutouts of 2'  $\times$  2' fields centred on the S10 QSO positions. This field size is sufficient since all but 7 of our radio-detected quasars have smaller angular sizes than 2' (see e.g., de Vries et al. 2006), which corresponds to pro-

<sup>3</sup> Most of these FIRST-detected colour-selected quasars are associated with single radio counterparts within 10'' of the optical

position. Only 4% of the FrQSOs have multiple radio components, whilst 8% of the FbQSOs and 10% of the FcQSOs have multiple radio components.



**Figure 8.** The FIRST 1.4 GHz radio-detection fraction as a function of redshift for the blue (bQSOs), control (cQSOs) and red (rQSOs) quasars using the colour scheme in Figure 2; we also plot on the radio-detection fraction for non-red QSOs, which is defined as all quasars excluding the rQSOs. The data are taken from Table 3 and the errorbars correspond to the  $1\sigma$  binomial uncertainties. The horizontal bars denote the redshift ranges of the four  $z$ -bins. The rQSOs have a factor  $\approx 2$ –3 times larger radio-detection fraction in comparison to the bQSOs and cQSOs. The shaded regions represent the FIRST detection rates for the  $L_{6\mu\text{m}} - z$  matched bQSOs, cQSOs and rQSOs.

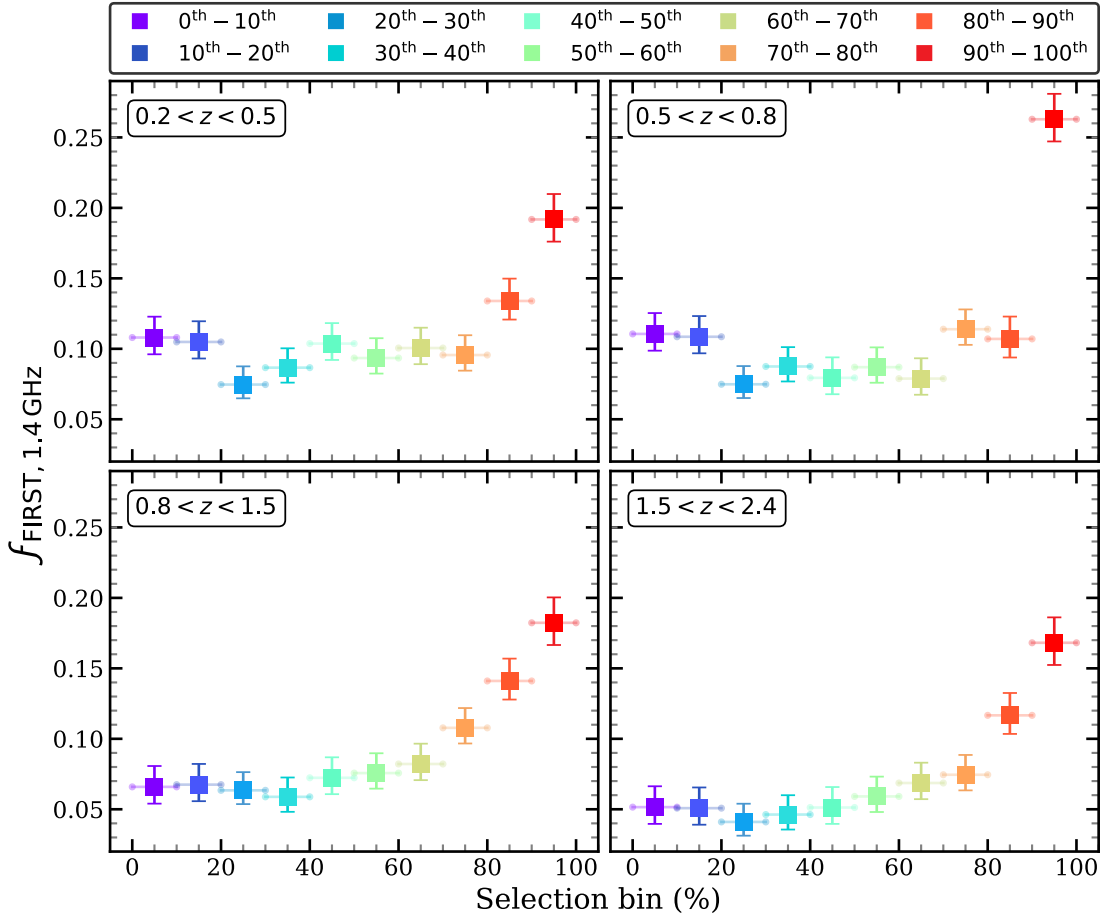
jected sizes of  $< 0.4$ – $1.0$  Mpc at  $z = 0.2$ – $2.4$ . In our visual assessment we employed a simplified classification scheme that captures the main morphological classes of radio-detected quasars and minimises redshift- and resolution-dependent effects: (1) faint, (2) compact, (3) extended, (4) FR II-like and (5) compact FR II; see Table 4 for a more detailed description. Of all the FIRST-detected quasars in our study, 27% required visual assessment according to our approach with the remaining 73% of radio-detected quasars categorized either as compact (non-extended; single components with fitted major axes less than  $5''$ ) or faint ( $F_{\text{peak}} < 3$  mJy) radio sources. Although the compact and faint radio sources are not expected to be extended, for completeness we performed a visual check of their morphologies: we found 5% of the faint and compact samples to have either extended or FR II-like morphologies and we reclassified these systems.

Figure 12 summarizes the results of our morphological analysis by showing the percentages of the bQSOs, cQSOs and rQSOs in each of the morphology classes; see also

Table 5. We calculated the  $1\sigma$  binomial uncertainties on our percentages for both the full and  $L_{6\mu\text{m}} - z$  matched colour-selected samples following Cameron (2011). This figure shows that rQSOs have a different radio morphological mix to blue quasars. There are no significant differences in the fraction of rQSOs and blue quasars with extended radio morphologies, such as the classical FR II-type systems. However, a factor 2–6 more rQSOs have either compact radio emission or are radio faint, in comparison to blue quasars, a result that is consistent between both the full and  $L_{6\mu\text{m}} - z$  matched colour-selected samples. It is these compact and faint radio sources that are responsible for the increase in the overall radio-detection fraction between rQSOs and blue quasars in Figure 8.

### 3.3 Radio luminosities of red versus blue quasars

The excess of faint radio detections in red quasars compared to blue quasars suggests that a larger fraction of



**Figure 9.** The FIRST 1.4 GHz radio-detection fraction as a function of the  $g^* - i^*$  quantile split into 10% selection bins in the four respective redshift bins. The top 10% of the reddest SDSS quasars always show the largest radio-detection fraction.

**Table 4.** The radio morphology classes used to classify the FIRST images for the radio-detected quasars.

Classification	Description
Faint	Sources detected close to the FIRST detection threshold with peak fluxes of $F_{\text{peak}} < 3$ mJy.
Compact	Sources that are point-like with non-extended emission (fitted major axes $< 5''$ ).
Extended	Single radio sources that are extended. This class includes FRI-like systems where both lobes are fainter than the core; $F_{\text{lobe}} < F_{\text{peak}}$ .
FRII-like	Double lobed systems with approximately the same brightness and offset from QSO position. At least one lobe should be brighter than than QSO core ( $F_{\text{lobe}} > F_{\text{peak}}$ ).
Compact FRII	FRII-like systems on small scales, i.e within the $10''$ radius circle (which corresponds to a projected size of $\sim 85$ kpc at $z = 1.5$ ).

FrQSOs have low radio luminosities. In addition to the radio morphologies we therefore also explored the radio luminosities ( $L_{1.4\text{GHz}}$ ) and “radio-loudness” (here defined as  $L_{1.4\text{GHz}}/L_{6\mu\text{m}}$ ) of the FIRST-detected quasars. For consistency, in these analyses we used the total FIRST fluxes of all radio-detected components within  $10''$  to calculate the 1.4 GHz luminosities, even if their NVSS fluxes differed from FIRST (see §2.1.2).

In Figure 13 we plot  $L_{1.4\text{GHz}}$  vs. redshift for the FbQSOs, FcQSOs and FrQSOs. The radio luminosity distribu-

tions of all three samples changes with redshift due to the flux limit of the FIRST survey. Beyond  $z > 0.5$ ,  $L_{1.4\text{GHz}}$  is higher than that of the strongest star-forming galaxies, indicating that the radio emission must be dominated by the AGN in almost all cases (e.g., Arp 220 is the most powerful nearby starburst with  $\log(L_{1.4\text{GHz}}/\text{W Hz}^{-1}) = 23.4$ ; Condon et al. 2013). Noticeably, as indicated by our morphology analysis, there is a strong concentration of FrQSOs close to the FIRST detection limit.

An alternative way to investigate the radio power is to

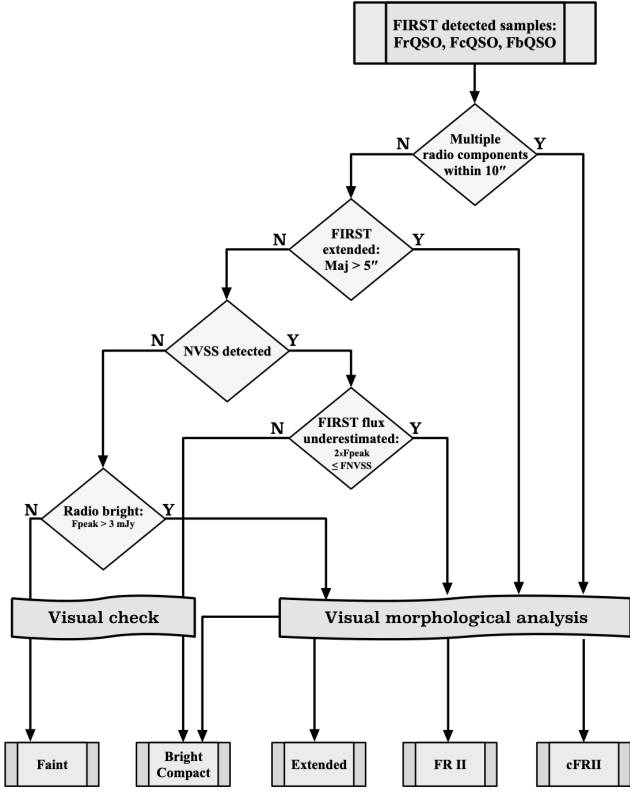


**Figure 10.** Schematic flow diagram of our radio morphology classification for the FrQSOs, FcQSOs and FbQSOs. Four subcategories were selected to be visually assessed to accurately determine the morphological class. For completeness we also visually checked all of the other radio-detected quasars.

**Table 5.** The number and percentage of quasars in each of the morphology classes described in Table 4; see Figure 12.

Classification	bQSO	cQSO	rQSO
The number of quasars in each class:			
Faint	73	97	357
Compact	142	107	348
Extended	86	67	69
FR II-like	33	34	32
Compact FR II	6	10	10
The percentage in each class (see Figure 12):			
	(%)	(%)	(%)
Faint	$1.49^{+0.193}_{-0.153}$	$1.98^{+0.218}_{-0.179}$	$7.287^{+0.387}_{-0.352}$
Compact	$2.898^{+0.258}_{-0.22}$	$2.184^{+0.228}_{-0.189}$	$7.103^{+0.383}_{-0.348}$
Extended	$1.755^{+0.207}_{-0.168}$	$1.368^{+0.186}_{-0.146}$	$1.408^{+0.188}_{-0.148}$
FR II-like	$0.673^{+0.137}_{-0.097}$	$0.694^{+0.139}_{-0.099}$	$0.653^{+0.136}_{-0.096}$
Compact FR II	$0.122^{+0.073}_{-0.032}$	$0.204^{+0.086}_{-0.046}$	$0.204^{+0.086}_{-0.046}$

explore the relative ratio of the quasar in the radio band to the overall accretion power. This is effectively a measure of the “radio loudness”, which we define here as  $R$ . Many studies use the 5 GHz-to-2500 Å flux ratio to define radio-loud quasars as objects with  $R > 10$  (e.g., Kellermann et al. 1989; Stocke et al. 1992; Urry & Padovani 1995; Ivezić et al. 2002; Glikman et al. 2004; Zakamska & Greene 2014; Mehdipour & Costantini 2019). The transition between the radio-quiet and radio-loud regime is not definite and often quasars with  $3 < R < 100$  are considered to be radio-intermediate. Using the  $R$ -values provided in Shen et al. (2011) and the standard definition of radio loudness, we find that 81%, 78% and 83% of the FbQSOs, FcQSOs and FrQSOs are radio-loud quasars with  $R > 10$ .

To reliably constrain the radio loudness in our analyses here we use the rest-frame 1.4 GHz–6 μm luminosity ratio ( $L_{1.4\text{GHz}}/L_{6\mu\text{m}}$ ), which will be less affected by dust extinction and redshift effects. In Figure 14 we plot the relative fraction of FrQSOs and FbQSOs compared to FcQSOs as a function of  $R$  for both the full (filled markers) and  $L_{6\mu\text{m}}-z$  matched (shaded regions) colour-selected samples. We estimate the transition between radio-quiet and radio-loud quasars by requiring that 90% of the Shen et al. (2011) identified radio-loud FcQSOs satisfies our radio loudness definition:  $\log_{10}(L_{1.4\text{GHz}}/L_{6\mu\text{m}}) \approx -4.2$  (dot-dashed line); we used the FcQSOs since they will have typical optical quasar colours unaffected by dust reddening. This figure shows a factor  $\approx 3-4$  enhancement in the fraction of FrQSOs with respect to both FbQSOs and FcQSOs towards lower values of  $R$ , indicating that the enhanced radio-detection fraction for the FrQSOs is from systems around the radio-loud–radio-quiet threshold; we quantified this threshold ( $\log_{10}(L_{1.4\text{GHz}}/L_{6\mu\text{m}}) \approx -4.2$ ) in terms of the mechanical-to-radiative power to be  $P_{\text{mech, sync}}/P_{\text{rad, } L_{6\mu\text{m}}} \approx 0.001$ .<sup>4</sup> As may be expected, given our earlier radio-morphology results, the enhancement in the fraction of rQSOs at low  $R$  values comes from systems with either faint or compact radio morphologies; the number of sources in each bin are indicated in Figure 14 and tabulated in Table 6. No significant differences are found between red and blue quasars within the classical extended radio-loud systems.

## 4 DISCUSSION

We have analysed the SDSS DR7 Quasar Catalogue from S10 to look for fundamental differences in the radio properties between red and blue quasars. By carefully selecting rQSOs, cQSOs and bQSOs from the top, middle and bottom 10% of the observed  $g^* - i^*$  colour distributions we have generated uniformly selected samples unbiased in their radio properties. Overall, we have found that rQSOs have a FIRST radio-detection fraction of  $\approx 15 - 20\%$ , which is a factor of

<sup>4</sup> On the basis of the methodology given in Willott et al. (1999), we calculate the mechanical power from the jet and find that for our assumed radio quiet-radio loud threshold the mechanical-to-radiative power ( $P_{\text{mech, sync}}/P_{\text{rad, } L_{6\mu\text{m}}}$ ) corresponds to  $\sim 0.1\%$ . In this calculation we assume a normalization factor  $F_W = 5$  (see Daly et al. 2012); the normalization factor ranges between 1–20, and combines several factors such as the lobe filling factor and the amount of energy from non-radiating particles.

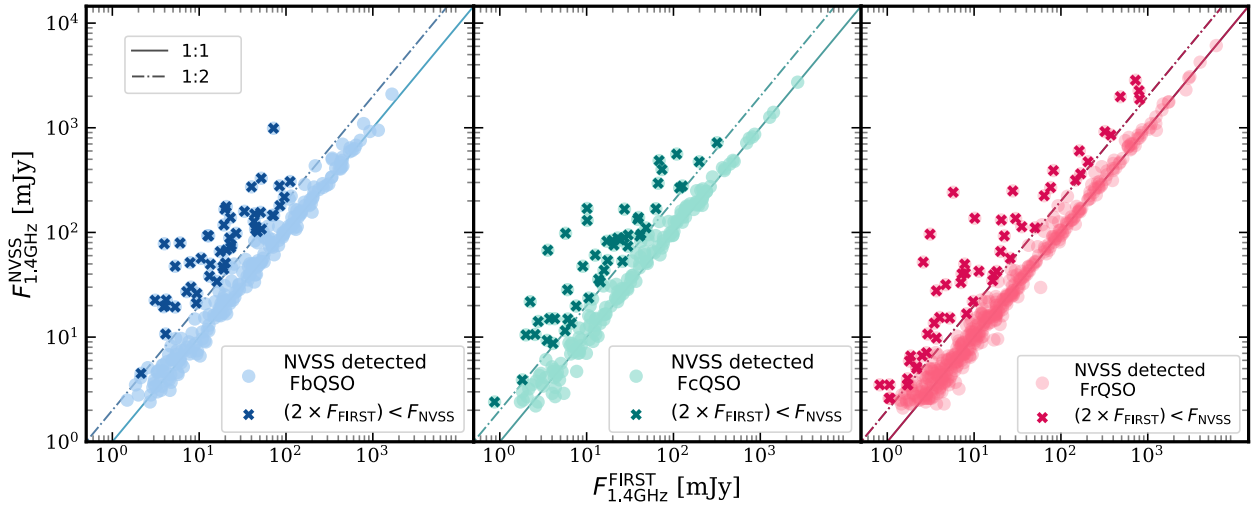


**Figure 11.** NVSS flux vs. FIRST flux at 1.4 GHz for the NVSS detected FbQSO, FcQSO and FrQSO indicated with faded blue, green and red circles. Sources with underestimated FIRST fluxes are indicated with dark blue, green and red crosses. The solid lines indicate a 1:1 relation and the dash-dot lines a 1:2 relation.

**Table 6.** The number of FbQSOs, FcQSOs and FrQSOs in the bins of  $\log_{10}(L_{1.4\text{GHz}}/L_{6\mu\text{m}})$  plotted in Figure 14. Each bin is subdivided into our radio morphology classes; faint, compact and extended sources (extended, FR II and compact FR II).

$\log_{10}(L_{1.4\text{GHz}}/L_{6\mu\text{m}})$	Sample	Faint	Compact	Extended
-4.75	FbQSO	53	14	7
	FcQSO	84	16	11
	FrQSO	321	63	13
-3.75	FbQSO	17	26	29
	FcQSO	11	25	16
	FrQSO	33	108	27
-3.25	FbQSO	2	41	39
	FcQSO	0	26	34
	FrQSO	0	85	27
-2.25	FbQSO	0	61	50
	FcQSO	0	40	50
	FrQSO	0	87	43

$\approx 2 - 3$  times larger than that of blue quasars (cQSOs and bQSOs). Through a visual inspection of the FIRST images and an assessment of the radio luminosities ( $L_{1.4\text{GHz}}$  and  $L_{1.4\text{GHz}}/L_{6\mu\text{m}}$ ) we find that the radio-detection excess for rQSOs is primarily due to compact and radio-faint quasars (those around the radio quiet-radio loud threshold). No significant differences are found between rQSOs, cQSOs, and bQSOs within the classical extended radio-loud systems. We find consistent results between our full and  $L_{6\mu\text{m}}-z$  matched colour-selected samples. Given that the radio luminosities of the quasars are at least an order of magnitude above those expected from star-formation (e.g.,  $L_{1.4\text{GHz}} > 10^{25} \text{ W Hz}^{-1}$  at  $z > 1.5$ ), the differences in the radio properties will be driven by AGN-related processes (e.g., radio core, jets, lobes, winds).

Many previous studies have explored the optical properties of radio-detected quasars, finding that they tend to have redder optical colours than radio-undetected quasars (e.g., Ivezic et al. 2002; White et al. 2003). While other studies have explored the radio morphologies of radio-detected quasars and found that the quasars with unresolved radio emission tend to have redder optical colours than the quasars with extended radio emission (e.g., Lu et al. 2007; Kimball et al. 2011). However, fewer studies have explored the radio properties of carefully selected red and blue quasars. Tsai & Hwang (2017) distinguished between red and blue quasars based on their spectral colours (flux ratio of the rest frame  $4000\text{\AA}$  to  $3000\text{\AA}$  continuum emission) and, similarly to our work, found a larger number of red quasars to be detected with FIRST; however, their analysis was restricted to low redshifts ( $0.3 < z < 1.2$ ). Similarly, Richards et al. (2003) reported that dust-reddened SDSS quasars have average FIRST detection-fractions  $\approx 2 \times$  larger than intrinsically blue quasars while White et al. (2007) stacked the FIRST data of SDSS quasars as a function of  $g^* - r^*$  colour and found an increase in the radio-flux density towards redder optical colours. We also note that Georgakakis et al. (2009) tentatively found that a higher fraction of 2MASS NIR selected quasars are associated with radio emission than optically selected SDSS quasars.

However, our study is the first to systematically explore the optical colour dependence on the radio-detection fraction as a function of radio morphology, luminosity, and “radio-loudness”. A strength of our approach is that we have carefully selected comparison samples (rQSO, cQSO, and bQSO) from the same quasar population, allowing us to rule out significant selection and luminosity effects in our analyses.

Overall, given the connection between the rQSOs and radio emission it is natural to ask whether they are produced by the same physical process. The only process likely to contribute to both the optical and radio wavebands is synchrotron radiation, which is the dominant physical mechanism in the radio waveband. Qualitatively, it appears un-

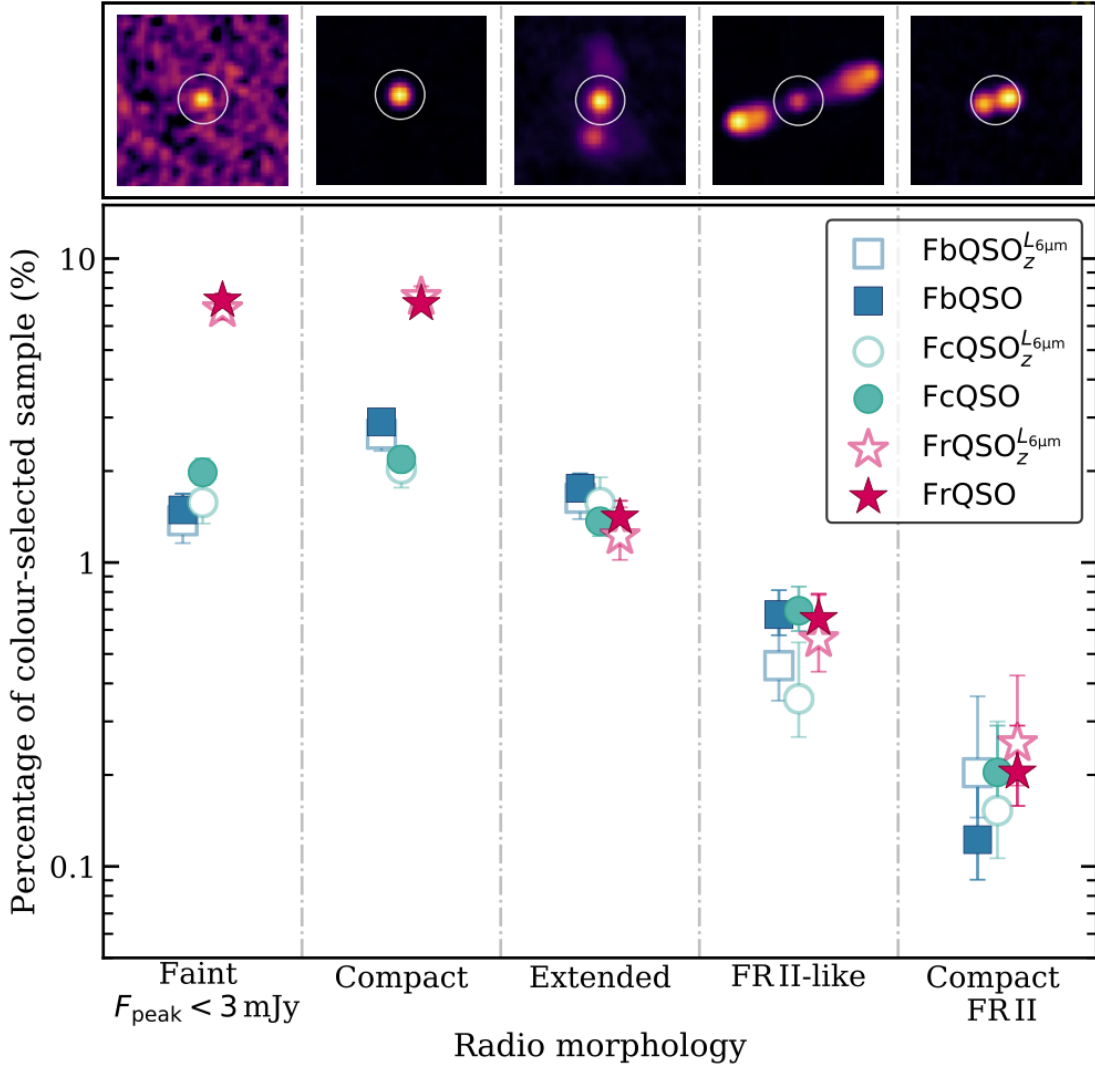


**Figure 12.** The percentage of both the full colour-selected (filled markers) and the  $L_{6\mu m} - z$  matched (open markers) samples (using the colour scheme in Figure 2) with different radio morphologies. The fractions are reported in five categories: faint sources detected near the sensitivity limit ( $F_{\text{peak}} < 3 \text{ mJy}$ ), bright compact radio sources, bright extended radio sources, FR II-like systems and compact FR IIs (small scale lobe-systems); see Table 4 for more details. The errorbars correspond to the  $1\sigma$  binomial uncertainties and the vertical dash lines separate the different categories. Example  $2' \times 2'$  FIRST images of each morphological class are illustrated in the top panel. The white circle represents our cross-matching radius of  $10''$ . Extended radio emission is found among a similar fraction of all quasars, but red quasars show a surfeit of compact and faint systems.

likely that synchrotron radiation can explain the enhanced radio emission in rQSOs since the significant difference between rQSOs and blue quasars occurs in comparatively radio-weak systems. Indeed, from a more quantitative analysis, where we scale a synchrotron-dominated SED to the radio flux, we predict that only  $\approx 6\%$  of the FbQSOs and FcQSOs and  $\approx 8\%$  of FrQSOs are likely to suffer from significant contamination of the optical emission from synchrotron processes; see appendix A for more details. Our results are qualitatively similar to those of Glikman et al. (2007) who undertook a similar analysis but for a brighter NIR selected red-quasar sample. We therefore conclude that dust extinction is the most plausible explanation for the optical colours of the majority of red quasars, in agreement with previous works (e.g., Webster et al. 1995; Gregg et al. 2002; Richards et al. 2003; Glikman et al. 2004, 2007, 2012; Kim & Im 2018),

particularly at  $z > 0.5$  where dilution from the host galaxy is likely to be weak (see §2.3.1).

On the basis of our results how can we explain the connection between the red colours and different radio properties of the rQSOs when compared to blue quasars? Below we discuss our results within the context of the two competing models for red quasars, the orientation model (§4.1) and the evolutionary model (§4.2).

#### 4.1 Evidence against a simple orientation-dependent model

In a simple orientation-dependent model we would not expect physical differences between red and blue quasars; in this model any observed differences would merely be a consequence of more dust along the line-of-sight. Since radio

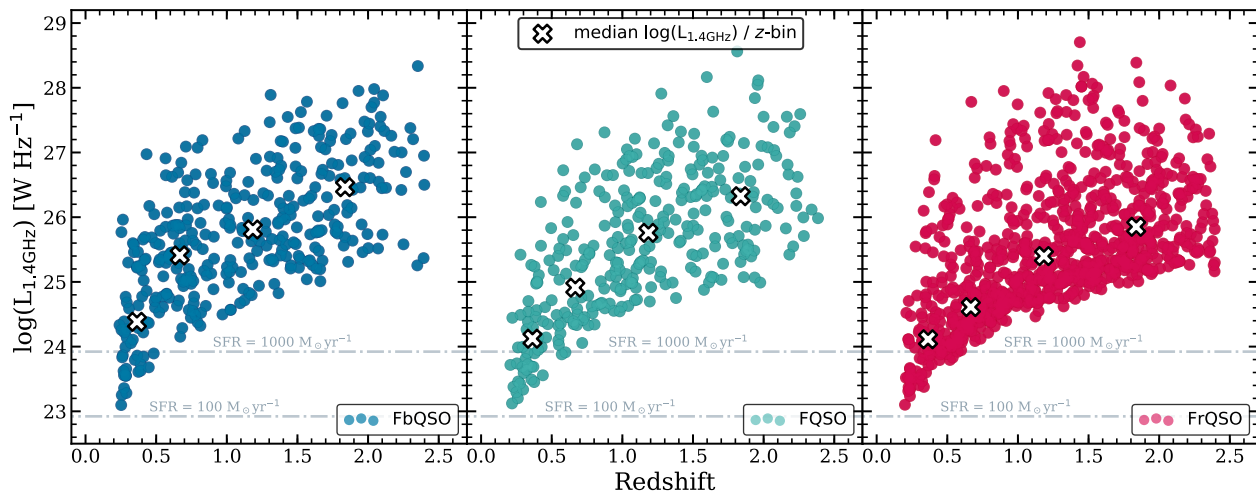


**Figure 13.** Radio luminosity at 1.4 GHz versus redshift for the radio-detected FbQSO (left), FcQSO (middle) and FrQSO (right) quasars. The FIRST fluxes of quasars with multiple radio counterparts within  $10''$  have been added to compute the total luminosity. The median  $\log(L_{1.4\text{GHz}})$  in each of the 4 redshift bins are indicated with crosses. The dash-dot lines indicate radio luminosities corresponding to star formation rates (SFRs) of 100 and  $1000 M_{\odot} \text{yr}^{-1}$  (see Hopkins et al. 2001, for details on the SFR calculations).

emission is not affected by dust, we would therefore expect no significant differences in the radio-detection fraction between different quasar sub populations, in stark contrast to our result (factor  $\approx 3$  times more radio-detected rQSOs when compared to bQSOs and cQSOs, even when controlling for luminosity and redshift effects). In fact, since blue quasars would be more face on than the red quasars, on the basis of the orientation model, we would actually expect the opposite result (i.e., a relatively larger fraction of radio-detected bQSOs and cQSOs than rQSOs).

The differences in the radio morphologies and the radio luminosities of the rQSOs and blue quasars also argue against the orientation model. In the orientation model the rQSOs are more inclined than blue quasars and so the radio emission would be more extended (on average) while we find an excess of compact radio morphologies for the rQSOs, again the opposite to what we would expect. The larger fraction of rQSOs with low radio luminosities (i.e., either  $L_{1.4 \text{ GHz}}$  or  $L_{1.4 \text{ GHz}}/L_{6\mu\text{m}}$ ) is also inconsistent with the orientation model which would predict no significant differences in the radio luminosities of the different quasar sub populations.

#### 4.2 Empirical constraints for an evolutionary model

Since our radio results cannot be explained (solely) by orientation, they must imply fundamental differences between red and blue quasars. These differences could be driven by changes in the physical properties of the quasars themselves (e.g., the BH accretion disc) or they could be related to the larger-scale “environment”; we use the term “environment” here to describe a broad range of potential physical phenomena over a wide range of size scales (e.g., pc–Mpc scales). We briefly discuss the empirical constraints that our study can place on these scenarios below.

Several studies have found that a small number of X-ray, optical, and NIR selected quasars are characterized by

intrinsically red continua, potentially related to different accretion rates in the red quasars compared to blue quasars (Puchnarewicz & Mason 1998; Richards et al. 2003; Young et al. 2008; Ruiz et al. 2014; Kim & Im 2018). Since it has also been noted that radio emission is enhanced in low Eddington rate AGN (e.g. Heckman et al. 2004; Kauffmann et al. 2008), it is therefore reasonable to consider whether the rQSOs have lower accretion rates in comparison to bQSOs and cQSOs due to their enhanced radio-detection fractions. We test this here by estimating the range in Eddington ratios between the  $L_{6\mu\text{m}} - z$  matched colour samples using the bolometric luminosities (estimated from  $L_{6\mu\text{m}}$ ; see §2.3.1) and the FWHM of the broad lines as a proxy of the BH masses (i.e., based on virial BH masses).

In Figure 15 we show the estimated bolometric luminosity ( $L_{\text{bol},6\mu\text{m}}$ ) as a function of FWHM for the b,c,rQSO $^L_{6\mu\text{m}}$  quasars. The median values for the different broad lines (different  $z$ -bins) are overlaid and we calculated the median absolute deviation (MAD) as the uncertainty on the median. Eddington ratio tracks ranging from  $0.01 < \lambda_{\text{Edd}} < 1$  are also plotted, calibrated against values from Shen et al. (2011) for the cQSOs. A large scatter in the FWHMs is observed, especially for the rQSOs which often have larger associated uncertainties due to lower SNR spectra. Nevertheless, from the median values it is clear that there are no statistically significant differences in the FWHM values between the b,c,rQSO $^L_{6\mu\text{m}}$  quasars. These results would appear to be in disagreement with Richards et al. (2003) who found a trend of narrower Balmer lines towards redder optical colours; however, we note that this result is based on composite quasar spectra with higher SNR allowing them to see more subtle trends than in our analysis. Using the bolometric and BH mass relation for the Eddington ratio, we estimated the median Eddington ratio for each bin of the bQSOs, cQSOs, and rQSOs: all are broadly consistent with an increase from low-to-high redshift of  $\lambda_{\text{Edd}} \approx 0.1 - 0.5$ . Since the quasars are matched in luminosity we therefore argue that there are no strong differences in the *average*



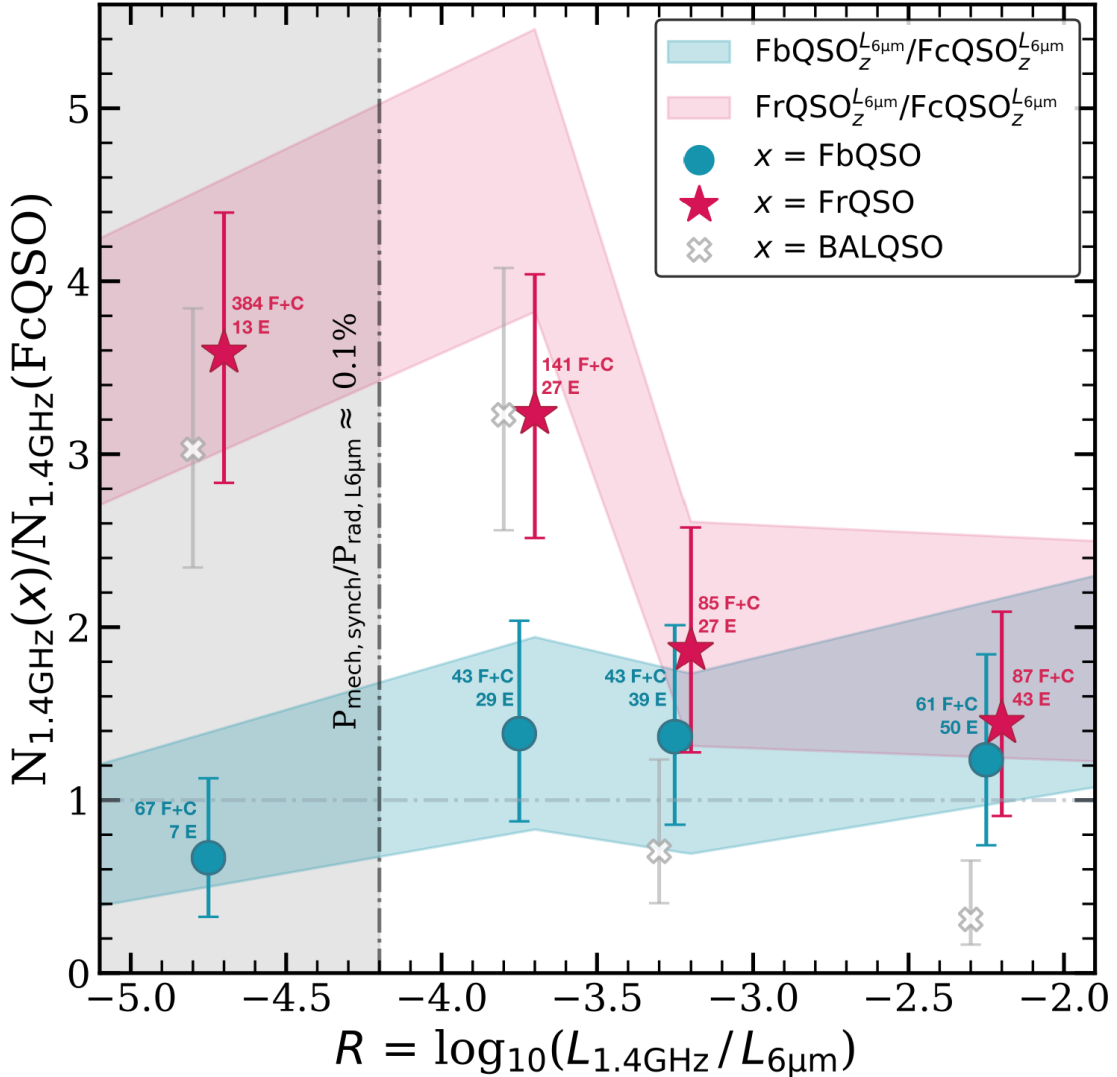


**Figure 14.** The FIRST 1.4 GHz radio-detection fraction in bins of radio loudness, computed using the 1.4 GHz and  $6\mu\text{m}$  luminosities, of the full (coloured markers) and  $L_{6\mu\text{m}} - z$  matched (coloured shaded regions) colour samples. The relative fraction of FIRST-detected CIV BALQSOs compared to FcQSOs at  $1.5 < z < 2.4$  are also plotted as a function of  $R$  (grey crosses; see §4.2). The blue, red and grey markers are offset for illustration purposes. The grey shaded region indicates the radio-quiet regime and the dashed-dot line show the transition between radio-quiet and radio-loud quasars, quantified in terms of the mechanical-to-radiative power (see footnote 4 and §3.3). The number of sources in each  $R$ -bin is subdivided into faint and compact morphologies (F+C) and extended (E; including extended, FR IIs and compact FR IIs) morphologies. The enhanced radio-detection fraction for the rQSOs is predominantly from systems around the radio-quiet-radio loud threshold with faint or compact radio morphologies.

accretion rates between red and blue quasars. This result appears to be in disagreement with some previous studies which have found that radio-selected red quasars have higher accretion rates than blue quasars (e.g., Urrutia et al. 2012; Kim et al. 2015), on the basis of optical–NIR spectra of small quasar samples. However, our current analysis is limited by the large uncertainties in individual FWHM measurements from Shen et al. (2011). We aim to clarify the connection between red quasars and accretion properties in upcoming work using a matched sample of rQSOs and cQSOs with high-quality VLT-XSHOOTER optical–NIR spectroscopy.

While our analyses of the accretion properties do not show significant differences between the red and blue quasars *on average*, the enhancement in the fraction of rQSOs with

compact or faint radio emission suggest fundamental differences between these sub populations. The radio compactness indicates that the source of the differences in the radio properties emerges on nuclear or galaxy scales ( $< 40$  kpc). Within the context of the evolutionary model, this could imply that the red quasars are in a younger transitional phase with small, but expanding, radio jets (such as Compact Steep Spectrum (CSS) and gigahertz-peaked spectrum (GPS); see also e.g., O’Dea & Baum 1997; Murgia et al. 1999; Rossetti et al. 2006; Randall et al. 2011; Dallacasa et al. 2013; Orienti 2016); indeed, Georgakakis et al. (2012) has argued a similar interpretation for a small sample of FIRST-detected dust-reddened quasars. In this model red quasars represent an early obscured phase during which energetic winds drive

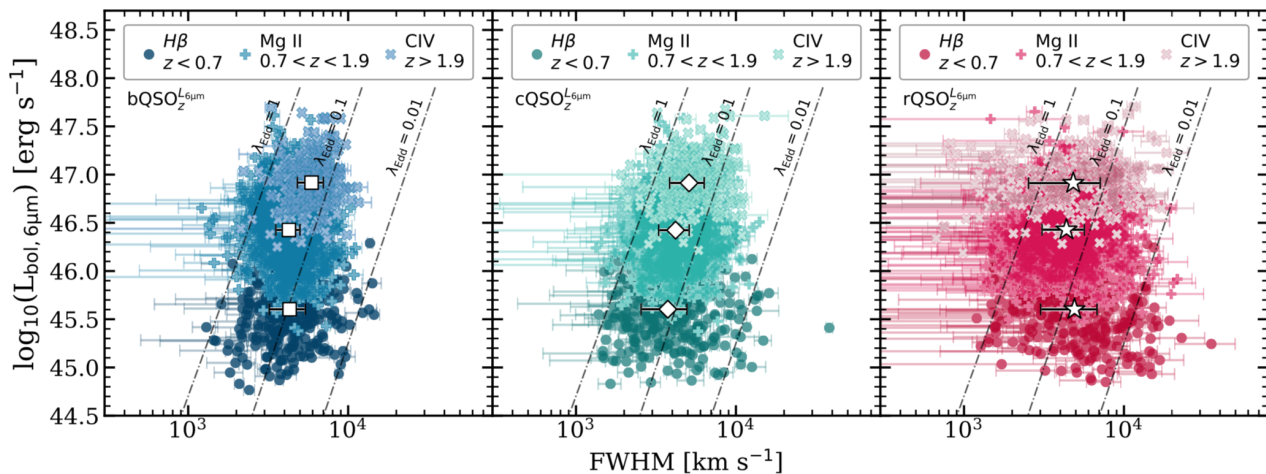


**Figure 15.** The bolometric luminosity estimated using the  $L_{6\mu\text{m}}$  vs. FWHM of the broad-lines H $\beta$  (circles), Mg II (crosses) and C IV (X's) of the b,c,rQSO $_z^{L_{6\mu\text{m}}}$  quasars. The median values and median absolute deviations (MAD) are plotted for each emission line. Also plotted are Eddington ratio tracks (dash-dot grey lines) determined from the Eddington ratios provided Shen et al. (2011) for the cQSOs (since they represent typical quasars). There are no strong differences in the FWHM measurements and implied Eddington ratios between the red quasars and blue quasars.

away the obscuring dust and gas revealing an unobscured view of the accretion disc (i.e., a blue quasar). As the dust cocoon expands it confines a young radio source which remains compact on galaxy scales. Strong shocks associated with these interactions could sustain their radio synchrotron emission (e.g., Hwang et al. 2018), leading to the enhanced radio-detection fractions which we observe.

A prediction of the evolutionary model is that red quasars will host more powerful winds than blue quasars. Interestingly, Mehdipour & Costantini (2019) recently showed an anti-correlation between the column density of ionised winds in quasars and the “radio-loudness”, whereby the systems with the weaker radio emission have stronger winds. The enhancement in the fraction of rQSOs with low  $R = L_{1.4\text{ GHz}}/L_{6\mu\text{m}}$  values therefore indirectly suggests that they will host stronger winds than bQSOs. On the basis of the current data, we are unable to test whether the rQSOs have stronger winds than the bQSOs. However, we can use the sub population of broad absorption line quasars (BALQSOs; Foltz et al. 1987; Weymann et al. 1991), which are known to host powerful winds, to see whether they are preferentially radio weak and to therefore provide an indirect test of this relationship. In Figure 14 we plot the relative fraction of FIRST-detected BALQSOs compared to FcQSOs as a function of  $R$ ; we identified BALQSOs as systems with C IV ( $1.5 < z < 2.4$ ) broad absorption lines from our parent sample (see Figure 1) using the data provided in Shen et al. (2011) (BAL\_FLAG = 1 or BAL\_FLAG = 3). We find an enhancement of BALQSOs at low values of  $R$  and a deficiency at high values of  $R$ , results which are in general agreement with those obtained by Morabito et al. (2019) for deeper low-frequency LOFAR radio data. The behaviour at high values of  $R$  is strikingly similar to that found for the rQSOs, suggesting that rQSOs may also host powerful winds, in good agreement with the evolutionary model; see also Urrutia et al. (2009) for evidence of an enhancement of BALQSOs in the red-quasar population. We will more directly test this hypothesis in a future VLT-XSHOOTER spectroscopic

study and also determine whether the red quasars from our sample host more powerful winds than the blue quasars.

## 5 CONCLUSIONS

We have taken a novel approach to search for fundamental differences between red and blue quasars at  $0.2 < z < 2.4$  to allow us to test between the two main competing models: the unified orientation model and an evolutionary model. Our quasar selection is based on the SDSS survey and is uniformly selected and unbiased in the radio. We distinguished between red (rQSOs), control (cQSOs) and blue (bQSOs) quasars using carefully constructed  $g^* - i^*$  colour distributions as a function of redshift. Our rQSO selection is therefore sensitive to the redshift evolution of quasar SEDs. We found that the red colours of the rQSOs suggest that the majority require  $A_V \sim 0.1 - 0.5$  mag of dust reddening to the median cQSO to produce the observed optical colours.

From a systematic comparison of the radio properties of the rQSOs, cQSOs and bQSOs, we have identified fundamental differences that cannot be attributed to just the orientation model. Our results are consistent between our full and  $L_{6\mu\text{m}} - z$  matched colour-selected samples:

- **Enhanced radio emission from the AGN in rQSOs (see Figure 8):** a larger fraction of rQSOs (by a factor of 2–3) are detected in the 1.4 GHz FIRST survey when compared to cQSOs and bQSOs. The average FIRST detection rate across  $0.2 < z < 2.4$  are 5%–10% for the cQSOs and bQSOs and 15%–20% for the rQSOs. The radio luminosities are at least an order of magnitude above those expected from SF (e.g.,  $L_{1.4\text{GHz}} > 10^{25} \text{ W Hz}^{-1}$  at  $z > 1.5$ ), indicating that they are driven by AGN-related processes. See §3.1.
- **rQSOs have differences in their arcsecond-scale radio morphologies (see Figure 12):** from a visual assessment of the FIRST cutouts we have found that the incidence of systems with extended and FR II-like radio mor-

phologies among the rQSOs is the same as among the cQSOs/bQSOs, but they have a much higher incidence of faint and compact radio counterparts (by a factor of 2–6). The radio-detection enhancement of the rQSOs therefore occurs in the compact and faint radio sources rather than the classical extended radio-loud systems. See §3.2.

- **rQSOs have lower radio–MIR luminosity ratios** ( $L_{1.4\text{ GHz}}/L_{6\mu\text{m}}$ ; see Figure 14): we found a factor  $\approx 3$ –4 enhancement of rQSOs at low  $L_{1.4\text{ GHz}}/L_{6\mu\text{m}}$  values, around the radio quiet-radio loud threshold, when compared to cQSOs and bQSOs. These differences are dominated by the compact and faint radio sources that are responsible for the enhanced radio-detection fraction of rQSOs. We see no significant differences in the classical extended radio-loud systems. See §3.3.

By linking the enhanced radio-detection rates and dust extinction of rQSOs we conclude that these sources are not blue quasars with additional dust along the line-of-sight due to a larger viewing angle as a simple orientation model would predict. By comparison we argue that the radio properties of the rQSOs are consistent with the evolutionary paradigm where rQSOs contain younger, more compact radio sources, possibly in a brief transitional phase where powerful winds are driving away the obscuring gas and dust.

In future work we will investigate radio spectral indices with multi-frequency radio data, which provide a more comprehensive understanding of the radio properties of the rQSOs. We will also further explore the origin of redness in the rQSOs from optical–NIR spectral analysis, constrain the star-formation rates from the host galaxy using *Herschel*–ALMA far-IR and mm imaging, and search for merger-driven signatures from high spatial resolution optical–NIR imaging.

## 6 ACKNOWLEDGEMENTS

We would like to acknowledge Elizabeth Wetherell for her assistance in the original discovery of the enhanced radio-detection fraction for red quasars. We also thank the anonymous referee for their useful comments which greatly improved the presentation and discussion of the results. We would also like to express our gratitude to the following people for their concise feedback and contributions: Manda Banerji, Alastair Edge, Richard McMahon, Andrea Merloni, Adam D. Myers, Gordon T. Richards, Nicholas P. Ross and Benny Trakhtenbrot.

We acknowledge the Faculty of Science Durham Doctoral Scholarship (LK), the Science and Technology Facilities Council (DMA, DJR, through grant code ST/P000541/1), a European Union COFUND/Durham Junior Research Fellowship (EL, through EU grant agreement no. 609412) and the financial support from the Swiss National Science Foundation (SF).

Funding for the SDSS and SDSS-II has been provided by the Alfred P. Sloan Foundation, the Participating Institutions, the National Science Foundation, the U.S. Department of Energy, the National Aeronautics and Space Administration, the Japanese Monbukagakusho, the Max Planck Society, and the Higher Education Funding Council for England. The SDSS Web Site is <http://www.sdss.org/>.

The SDSS is managed by the Astrophysical Research Consortium for the Participating Institutions. The Participating Institutions are the American Museum of Natural History, Astrophysical Institute Potsdam, University of Basel, University of Cambridge, Case Western Reserve University, University of Chicago, Drexel University, Fermilab, the Institute for Advanced Study, the Japan Participation Group, Johns Hopkins University, the Joint Institute for Nuclear Astrophysics, the Kavli Institute for Particle Astrophysics and Cosmology, the Korean Scientist Group, the Chinese Academy of Sciences (LAMOST), Los Alamos National Laboratory, the Max-Planck-Institute for Astronomy (MPIA), the Max-Planck-Institute for Astrophysics (MPA), New Mexico State University, Ohio State University, University of Pittsburgh, University of Portsmouth, Princeton University, the United States Naval Observatory, and the University of Washington.

This publication makes use of data products from the Wide-field Infrared Survey Explorer, which is a joint project of the University of California, Los Angeles, and the Jet Propulsion Laboratory/California Institute of Technology, funded by the National Aeronautics and Space Administration.

The National Radio Astronomy Observatory is a facility of the National Science Foundation operated under cooperative agreement by Associated Universities, Inc.

## REFERENCES

- Adelman-McCarthy J. K., et al., 2006, *ApJS*, **162**, 38  
 Alexander D. M., Hickox R. C., 2012, *NewAR*, **56**, 93  
 Alexander D. M., et al., 2003, *AJ*, **125**, 383  
 Anderson S. F., et al., 2003, *AJ*, **126**, 2209  
 Antonucci R., 1993, *ARA&A*, **31**, 473  
 Assef R. J., et al., 2013, *ApJ*, **772**, 26  
 Banerji M., McMahon R. G., P. C., Alaghband-Zadeh S., Gonzalez-Solares E., Venemans B. P., Hawthorn M. J., 2012, *MNRAS*, **427**, 2275  
 Banerji M., Carilli C. L., Jones G., Wagg J., McMahon R. G., Hewett P. C., Alaghband-Zadeh S., Feruglio C., 2017, *MNRAS*, **465**, 4390  
 Barvainis R., Lehár J., Birkinshaw M., Falcke H., Blundell K. M., 2005, *ApJ*, **618**, 108  
 Becker R. H., White R. L., Helfand D. J., 1995, *ApJ*, **450**, 559  
 Becker R. H., Helfand D. J., White R. L., Gregg M. D., Laurent-Muehlheisen S. A., 2012, *VizieR Online Data Catalog*, **8090**  
 Benn C. R., Vigotti M., Carballo R., Gonzalez-Serrano J. I., Sánchez S. F., 1998, *MNRAS*, **295**, 451  
 Bicknell G. V., 1995, *ApJS*, **101**, 29  
 Buchner J., Schulze S., Bauer F. E., 2017, *MNRAS*, **464**, 4545  
 Cameron E., 2011, *PASA*, **28**, 128  
 Condon J. J., Cotton W. D., Greisen E. W., Yin Q. F., Perley R. A., Taylor G. B., Broderick J. J., 1998, *AJ*, **115**, 1693  
 Condon J. J., Kellermann K. I., Kimball A. E., Ivezić Ž., Perley R. A., 2013, *ApJ*, **768**, 37  
 Cutri R. M., Nelson B. O., Kirkpatrick J. D., Huchra J. P., Smith P. S., 2001, in Clowes R., Adamson A., Bromage G., eds, *Astronomical Society of the Pacific Conference Series Vol. 232, The New Era of Wide Field Astronomy*. p. 78  
 Czerny B., Siemiginowska A., Janiuk A., Gupta A. C., 2008, *MNRAS*, **386**, 1557  
 Dallacasa D., Orienti M., Fanti C., Fanti R., Stanghellini C., 2013, *MNRAS*, **433**, 147

- Daly R. A., Sprinkle T. B., O’Dea C. P., Kharb P., Baum S. A., 2012, *MNRAS*, **423**, 2498
- Dermer C. D., Finke J. D., Krug H., Böttcher M., 2009, *ApJ*, **692**, 32
- Elvis M., et al., 1994, *ApJS*, **95**, 1
- Fanaroff B. L., Riley J. M., 1974, *MNRAS*, **167**, 31P
- Finke J. D., Dermer C. D., Böttcher M., 2008, *ApJ*, **686**, 181
- Foltz C. B., Weymann R. J., Morris S. L., Turnshek D. A., 1987, *ApJ*, **317**, 450
- Francis P. J., Whiting M. T., Webster R. L., 2000, *PASP*, **17**, 56
- Georgakakis A., Clements D. L., Bendo G., Rowan-Robinson M., Nandra K., Brotherton M. S., 2009, *MNRAS*, **394**, 533
- Georgakakis A., Grossi M., Afonso J., Hopkins A. M., 2012, *MNRAS*, **421**, 2223
- Glikman E., Gregg M. D., Lacy M., Helfand D. J., Becker R. H., White R. L., 2004, *ApJ*, **607**, 60
- Glikman E., Helfand D. J., White R. L., Becker R. H., Gregg M. D., Lacy M., 2007, *ApJ*, **667**, 673
- Glikman E., et al., 2012, *ApJ*, **757**, 51
- Glikman E., Simmons B., Maily M., Schawinski K., Urry C. M., Lacy M., 2015, *ApJ*, **806**, 218
- Glikman E., LaMassa S., Piconcelli E., Urry M., Lacy M., 2017, *ApJ*, **847**, 116
- Gregg M. D., Lacy M., White R. L., Glikman E., Helfand D., Becker R. H., Brotherton M. S., 2002, *ApJ*, **564**, 133
- Heckman T. M., Kauffmann G., Brinchmann J., Charlot S., Tremonti C., White S. D. M., 2004, *ApJ*, **613**, 109
- Heeschen D. S., Krichbaum T., Schalinski C. J., Witzel A., 1987, *AJ*, **94**, 1493
- Helfand D. J., White R. L., Becker R. H., 2015, *ApJ*, **801**, 26
- Hopkins A. M., Connolly A. J., Haarsma D. B., Cram L. E., 2001, *AJ*, **122**, 288
- Hopkins P. F., Hernquist L., Cox T. J., Kereš D., 2008, *ApJS*, **175**, 356
- Hwang H.-C., Zakamska N. L., Alexandroff R. M., Hamann F., Greene J. E., Perrotta S., Richards G. T., 2018, *MNRAS*, **477**, 830
- Ivezić Ž., et al., 2002, *AJ*, **124**, 2364
- Kauffmann G., Heckman T. M., Best P. N., 2008, *MNRAS*, **384**, 953
- Kellermann K. I., Sramek R., Schmidt M., Shaffer D. B., Green R., 1989, *AJ*, **98**, 1195
- Kim D.-W., Elvis M., 1999, *ApJ*, **516**, 9
- Kim D., Im M., 2018, *A&A*, **610**, A31
- Kim D., Im M., Glikman E., Woo J.-H., Urrutia T., 2015, *ApJ*, **812**, 66
- Kimball A. E., Ivezić Ž., 2008, *AJ*, **136**, 684
- Kimball A. E., Ivezić Ž., Wiita P. J., Schneider D. P., 2011, *AJ*, **141**, 182
- Klindt L., van Soelen B., Meintjes P. J., Väisänen P., 2017, *MNRAS*, **467**, 2537
- Kratzer R. M., Richards G. T., 2015, *AJ*, **149**, 61
- Kraus A., et al., 2003, *A&A*, **401**, 161
- LaMassa S. M., et al., 2016, *ApJ*, **820**, 70
- Lake S. E., Wright E. L., Petty S., Assef R. J., Jarrett T. H., Stanford S. A., Stern D., Tsai C.-W., 2012, *AJ*, **143**, 7
- Lu Y., Wang T., Zhou H., Wu J., 2007, *AJ*, **133**, 1615
- Mateos S., et al., 2012, *MNRAS*, **426**, 3271
- Mehdipour M., Costantini E., 2019, *A&A*, **625**, A25
- Morabito L. K., et al., 2019, *A&A*, **622**, A15
- Mullaney J. R., Alexander D. M., Goulding A. D., Hickox R. C., 2011, *MNRAS*, **414**, 1082
- Murgia M., Fanti C., Fanti R., Gregorini L., Klein U., Mack K.-H., Vigotti M., 1999, *A&A*, **345**, 769
- Muxlow T. W. B., Garrington S. T., 1991, Observations of large scale extragalactic jets. p. 52
- Netzer H., Lira P., Trakhtenbrot B., Shemmer O., Cury I., 2007, *ApJ*, **671**, 1256
- O’Dea C. P., Baum S. A., 1997, *AJ*, **113**, 148
- Orienti M., 2016, *Astronomische Nachrichten*, **337**, 9
- Park C., Song H., Einasto M., Lietzen H., Heinamaki P., 2015, *KAS*, **48**, 75
- Peterson B. M., 1997, An Introduction to Active Galactic Nuclei
- Prevot M. L., Lequeux J., Maurice E., Prevot L., Rocca-Volmerange B., 1984, *A&A*, **132**, 389
- Puchnarewicz E. M., Mason K. O., 1998, *MNRAS*, **293**, 243
- Randall K. E., Hopkins A. M., Norris R. P., Edwards P. G., 2011, *MNRAS*, **416**, 1135
- Richards G. T., et al., 2001, *AJ*, **121**, 2308
- Richards G. T., et al., 2002, *AJ*, **123**, 2945
- Richards G. T., et al., 2003, *AJ*, **126**, 1131
- Richards G. T., et al., 2006a, *AJ*, **131**, 2766
- Richards G. T., et al., 2006b, *ApJS*, **166**, 470
- Rieke G. H., Wisniewski W. Z., Lebofsky M. J., 1982, *ApJ*, **263**, 73
- Rose M., Tadhunter C. N., Holt J., Rodríguez Zaurín J., 2013, *MNRAS*, **432**, 2150
- Ross N. P., et al., 2015, *MNRAS*, **453**, 3932
- Rossetti A., Fanti C., Fanti R., Dallacasa D., Stanghellini C., 2006, *A&A*, **449**, 49
- Ruiz A., Della Ceca R., Caccianiga A., Severgnini P., Carrera F., 2014, in *The X-ray Universe 2014*. p. 314
- Sanders D. B., Soifer B. T., Elias J. H., Madore B. F., Matthews K., Neugebauer G., Scoville N. Z., 1988, *ApJ*, **325**, 74
- Schneider D. P., et al., 2005, *AJ*, **130**, 367
- Schneider D. P., et al., 2010, *AJ*, **139**, 2360
- Serjeant S., 1996, *Nature*, **379**, 304
- Shen Y., et al., 2007, *AJ*, **133**, 2222
- Shen Y., et al., 2011, *ApJS*, **194**, 45
- Stanley F., Harrison C. M., Alexander D. M., Swinbank A. M., Aird J. A., Del Moro A., Hickox R. C., Mullaney J. R., 2015, *MNRAS*, **453**, 591
- Stern D., et al., 2012, *ApJ*, **753**, 30
- Stoche J. T., Morris S. L., Weymann R. J., Foltz C. B., 1992, *ApJ*, **396**, 487
- Stoughton C., et al., 2002, *AJ*, **123**, 485
- Taylor M. B., 2005, in Shopbell P., Britton M., Ebert R., eds, *Astronomical Society of the Pacific Conference Series Vol. 347, Astronomical Data Analysis Software and Systems XIV*. p. 29
- Taylor M. B., 2006, in Gabriel C., Arviset C., Ponz D., Enrique S., eds, *Astronomical Society of the Pacific Conference Series Vol. 351, Astronomical Data Analysis Software and Systems XV*. p. 666
- Tsai A.-L., Hwang C.-Y., 2017, preprint ([arXiv:1705.06656](https://arxiv.org/abs/1705.06656))
- Urrutia T., Lacy M., Becker R. H., 2008, *ApJ*, **674**, 80
- Urrutia T., Becker R. H., White R. L., Glikman E., Lacy M., Hodge J., Gregg M. D., 2009, *ApJ*, **698**, 1095
- Urrutia T., Lacy M., Spoon H., Glikman E., Petric A., Schulz B., 2012, *ApJ*, **757**, 125
- Urry C. M., Padovani P., 1995, *PASP*, **107**, 803
- Vanden Berk D. E., et al., 2005, *AJ*, **129**, 2047
- Voges W., et al., 1999, *A&A*, **349**, 389
- Voges W., et al., 2000, *VizieR Online Data Catalog*, **9029**
- Wall J. V., 1975, *The Observatory*, **95**, 196
- Webster R. L., Francis P. J., Peterson B. A., Drinkwater M. J., Masci F. J., 1995, *Nature*, **375**, 469
- Weymann R. J., Morris S. L., Foltz C. B., Hewett P. C., 1991, *ApJ*, **373**, 23
- White R. L., Becker R. H., Helfand D. J., Gregg M. D., 1997, *ApJ*, **475**, 479
- White R. L., Helfand D. J., Becker R. H., Gregg M. D., Postman M., Lauer T. R., Oegerle W., 2003, *AJ*, **126**, 706
- White R. L., Helfand D. J., Becker R. H., Glikman E., de Vries W., 2007, *ApJ*, **654**, 99
- Whiting M. T., Webster R. L., Francis P. J., 2001, *MNRAS*, **323**, 718

- Wilkes B. J., Schmidt G. D., Cutri R. M., Ghosh H., Hines D. C., Nelson B., Smith P. S., 2002, *ApJ*, **564**, L65
- Willott C. J., Rawlings S., Blundell K. M., Lacy M., 1999, *MNRAS*, **309**, 1017
- Wright E. L., et al., 2010, *AJ*, **140**, 1868
- York D. G., et al., 2000, *AJ*, **120**, 1579
- Young M., Elvis M., Risaliti G., 2008, *ApJ*, **688**, 128
- Zakamska N. L., Greene J. E., 2014, *MNRAS*, **442**, 784
- de Vries W. H., Becker R. H., White R. L., 2006, *AJ*, **131**, 666

## APPENDIX A: CONTRIBUTION OF SYNCHROTRON RADIATION TO THE OPTICAL EMISSION

Here we estimate the contamination of the optical emission from synchrotron radiation for the radio-detected quasars to assess whether this can explain the enhancement in the radio-detection of rQSOs. The SEDs of compact radio sources such as FSRQs (which forms part of the blazar AGN subclass) are well known for their “double-humped” shape with a low-energy component extending from radio to UV/X-rays, and a high-energy component that extends from X-rays to GeV/TeV  $\gamma$ -rays. The synchrotron nature of the low-energy component is well established: FSRQs, for example, are well known for their low-synchrotron peaked SEDs with the peak frequency in the infrared regime ( $< 10^{14}$  Hz or wavelengths  $> 3\mu\text{m}$ ). Therefore, to investigate whether a red synchrotron component can explain the reddening of the rQSOs, we employed a model in which all the radio–optical power can be attributed to synchrotron emission, as in the case of FSRQs. If the rQSOs are reddened by dominant synchrotron emission beamed along our line-of-sight, we would expect the optical synchrotron fluxes to be in agreement with the observed optical fluxes.

The approach we have followed is to fit a synchrotron emission model (e.g., Finke et al. 2008; Dermer et al. 2009) to the radio–optical data of 3FGL J0045.2-3704 (see Klindt et al. 2017) to generate a prototypical template. We adopted the SED of 3FGL J0045.2-3704 because it has a blue quasar spectrum in the optical band, but also has a flat MIR–optical SED that is consistent with the observed properties of our quasars. We subsequently scaled this template to the 1.4 GHz flux of our radio-detected quasars to estimate their expected  $i$ -band flux from a synchrotron component. The ratios between the  $i$ -band fluxes estimated using the FSRQ synchrotron template ( $F_{i,\text{synch}}$ ) and the observed  $i$ -band SDSS fluxes ( $F_{i,\text{SDSS}}$ ) are shown in Figure A1 for the FIRST-detected bQSOs, cQSOs and rQSOs (FbQSOs, FcQSOs and FrQSOs, respectively).

For the majority of the quasars in all three samples a synchrotron model underpredicts the  $i$ -band fluxes by at least an order of magnitude. Only 6% of FbQSOs and FcQSOs and 8% of FrQSOs have  $F_{i,\text{synch}}$  greater than  $F_{i,\text{SDSS}}$ . This suggests that the optical bands are not contaminated by synchrotron emission from the radio jet for the majority of the radio-detected quasars in our sample and, hence, this cannot be the primary source of reddening of the rQSOs. Indeed, as can be seen in Figure A1, the majority of the rQSOs will have an extremely small synchrotron contribution to the optical emission, which is a direct consequence of the pre-ponderance of low radio luminosities from the rQSOs. Consequently, the majority of rQSOs are expected to have a

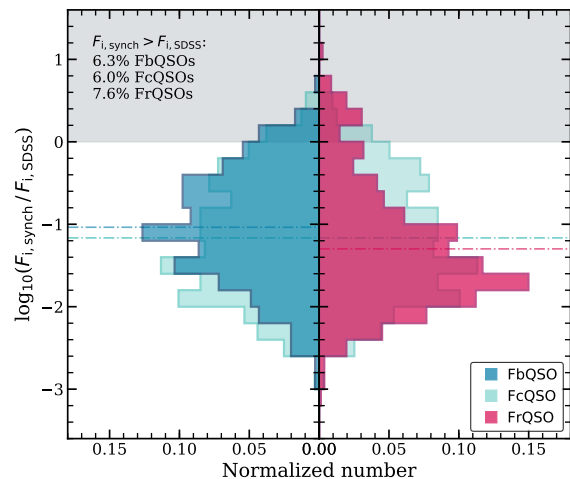


**Figure A1.** The ratio between the estimated synchrotron  $i$ -band flux and the observed SDSS  $i$ -band flux for the FbQSOs, FcQSOs and FrQSOs. The synchrotron  $i$ -band fluxes were estimated from the 1.4 GHz flux using a synchrotron model of an FSRQ, 3FGL J0045.2-3704. The dashed lines indicate the median for each distribution, and the grey shaded area indicates where  $F_{i,\text{synch}} > F_{i,\text{SDSS}}$ . Based on this it is evident that synchrotron emission is not the main source of reddening of the rQSOs.

lower synchrotron contribution in the optical band than the bQSOs and cQSOs.

This paper has been typeset from a  $\text{\TeX}/\text{\LaTeX}$  file prepared by the author.